RESIDUAL SERVICE LIFE PROGNOSTIC MODELS FOR TAPERED ROLLER BEARINGS

A Thesis

by

JENNIFER DANNI LIMA

Submitted to the Graduate College of
The University of Texas Rio Grande Valley
In partial fulfillment of the requirements for the degree of

MASTER OF SCIENCE IN ENGINEERING

May 2020

Major Subject: Mechanical Engineering

RESIDUAL SERVICE LIFE PROGNOSTIC MODELS FOR TAPERED ROLLER BEARINGS

A Thesis
by
JENNIFER DANNI LIMA

COMMITTEE MEMBERS

Dr. Constantine Tarawneh
Chair of Committee

Dr. Arturo Fuentes
Committee Member

Dr. Robert Jones
Committee Member

May 2020

ABSTRACT

Lima, JenniferD., Residual Service Life Prognostic Models for Tapered Roller Bearings. Master of Science (MS), May 2020, 87pp., 12 tables, 43 figures, 22 references.

There are a few different bearing health monitoring technologies currently used in the railroad industry, both reactive and preventative detection systems. Reactive models have proven to be ineffective in monitoring bearing health, which has resulted in either unnecessary train stoppages and delays or in-service failures and bearing burn-off leading to catastrophic train derailments. Wayside preventative detection systems, while more effective than reactive technologies, are scarce and neglect railcars' that do not travel over a specific route. This knowledge prompted the University Transportation Center for Railway Safety at UTRGV to develop an onboard bearing health monitoring system that can accurately assess the health of a bearing and identify the defective component at an early stage of the defect development. This system has been proven to accurately detect defective bearings through extensive laboratory testing validated by field testing performed at the Transportation Technology Center, Inc. in Pueblo, CO. Using this system, a prognostic model for the residual service life of a defective bearing was developed. This model can be used by the railroads to schedule proactive maintenance cycles to mitigate inefficient faulty bearing replacements.

DEDICATION

This thesis is dedicated to my family. To my father, who sparked in me a love for engineering. My older sister, Rossy, who always set a great example to follow. And my mother, Yolanda, for never giving up on me. I owe all my achievements to your love and support.

ACKNOWLEDGEMENTS

I don’t think I’m capable of expressing how grateful I am for my research director and mentor, Dr. Constantine Tarawneh. The dedication and tenacity that you show in all your endeavors is inspirational. You have provided me with so many things to be thankful for. You’ve helped me grow as a person and it is through your guidance that I have been able to accomplish so much. I found a second family at the University Transportation Center for Railway Safety. Thank you for believing me capable of obtaining my master’s degree and thank you for making a job feel like home.

I’d like to thank everybody from the UTCRS team. You guys are the best example of teamwork I’ve had the pleasure of seeing. I will always remember this time fondly and I know that all of you have a great future ahead.

I’d also like to show my appreciation for Dr. Fuentes and Dr. Jones, for their time and encouraging dispositions throughout the pursue of my Master’s degree. This could not have been accomplished without your aid. You are great professors and it is an honor to have been taught by you.

Finally, this study was made possible by funding provided by The University Transportation Center for Railway Safety (UTCRS), through a USDOT Grant No. #DTRT 13-G-UTC59.

DISCLAIMER

The contents of this thesis reflect the views of the authors, who are responsible for the facts and the accuracy of the information presented herein. This document is disseminated under the sponsorship of the U.S. Department of Transportation's University Transportation Centers Program, in the interest of information exchange. The U.S. Government assumes no liability for the contents or use thereof.

TABLE OF CONTENTS

LIST OF TABLES

LIST OF FIGURES

CHAPTER I

BACKGROUND & INTRODUCTION

1.1 Introduction

1.1.1 Tapered Roller Bearings

A typical freight car can weigh between 30 to 130 tons, depending on loading conditions. These loads are supported by various suspension components such as springs, dampers, wheels, axles, and tapered roller bearings. Railcars are equipped with two frontal and two rear wheel-axle assemblies, allowing for a total of eight tapered roller bearings per car. A single tapered roller bearing can sustain 16 ton loads and will undergo speeds of up to 129 km/h (80 mph).Due to the high travel velocities and heavy cargo loads experienced, bearing failure is in the top three leading causes for derailments [1].

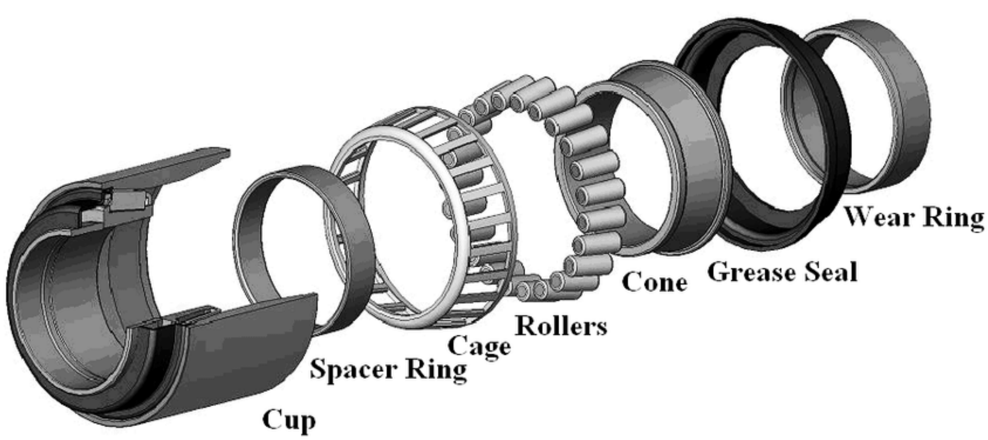

Figure 1. Components of a tapered roller bearing

The three primary components in a tapered roller bearing are the outer ring (cup), inner ring (cone) and rollers. The outer ring houses two inner rings. Each inner ring is surrounded by

23 rollers which are held together against the inner ring by a cage. Separating the cones is a spacer ring which varies in size depending on the bearing cup class. The Association of American Railroads (AAR) classifies bearings according to their size and load carrying capacity. The two principle bearing classes studied are class K and class F, their dimensions and loading conditions can be observed in Table 1, along with a few other common bearing classes. Seeing that Class F and Class K bearings share the same cup diameter they have identical nominal bearing loads and can use the same inner ring type.

Table 1. Bearing dimensions and loading conditions

Bearing Class	**Cup Dimension Diameter × Width [inch]**	**Bearing Load [kN] / [kips]**
E	6 × 11	117.0/26.3
F	6 ½ × 12	153.0/34.4
G	7 × 12	169.0/38.0
K	6 ½ × 9	153.0/34.4

The bearing outer ring (cup) is held stationary by the railcar load applied through the side frame. This creates a top loaded scenario as the one depicted in Figure 2. With the cupas a static element, it will experience constant forces as the movement-restricting loads are placed upon it. The cones, however, are able to rotate freely inside the cup, prompting this component to cycle in and out of the loaded zone. This cyclic loading results in the cone seeing smaller stresses and consequently less wear than that observed in the bearing cup. The rollers both rotate and revolve around the cone and thus see the least stress. These motions and varying load behaviors lead to the components having different spalling rates and defect development probabilities.

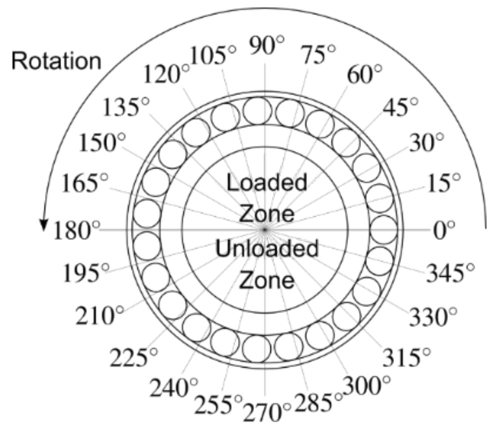

Figure 2. Schematic showing direction of rotation relative to loaded and unloaded zones

Bearing defects are categorized into three principle classifications: geometric, distributed, and localized. Geometric defects are caused by intolerances in the bearing geometry due to manufacturing errors. These defects are prone to causing high operation temperatures in a bearing without any visible signs of a surface flaw. A bearing is considered to have a distributed defect when a component has multiple imperfections along a raceway or when several components of the same bearing have developed a defect. An example of a distributed defect is shown in the water-etch inner ring in Figure 3 (right). Water-etch defects are caused by moisture entering the bearing, likely due to faulty seals. Once water enters, it commences a process of grease degradation which compromises the frictionless rotation common to a bearing and causes a sped abrasion rate in the components. Localized defects can be subcategorized into cracks, pits and spalls. Examples of spalling and pitting can be seen in Figure 3 (left).

Localized defects are primarily developed through the constant high stresses placed on subsurface inclusions of a steel component. Subsurface inclusions are caused by voids in the material or through impurities brought about by contaminants introduced during the manufacturing process. Through constant stress, the inclusions closer to the surface (within 400 μm below the raceway) will branch out and begin to chip away at the exterior. This type of failure is commonly known in the railroad industry as Rolling Contact Fatigue (RCF). Rolling

Contact Fatigue is the main mode of failure in a healthy and properly loaded bearing. Material fatigue is caused by contact stresses, in the example of a bearing it is caused by the rollers contact with the cup and cone raceways. Although material fatigue is primarily due to contact stresses, subsurface inclusions from material impurities can speed the defect development and propagation process.

Figure 3. Example of localized defects (left) and distributed defect (right)

1.1.2 Railway Safety

Once a defect develops on a bearing component, the near-frictionless rotational behavior of the bearing is compromised. The steel chipped off through propagation of subsurface inclusions will enter the grease and create a grinding effect on the component raceways as the lubricant continues to circulate through the bearing. Depending on the defect size, increased friction caused by coarse grease can predispose the bearing to frictional heating. The rise in bearing temperature creates a cycle of grease degradation which will cause further friction increase. Although the average calculated operating life of a bearing is more than 3 million kilometers [2], this estimation can drastically decrease in the presence of a developed defect. Unfortunately, defect development is highly variable and subject to the component material and manufacturing processes of the component. If not properly monitored, these defects can become catastrophic, leading to derailments or in-service failures.

1.2 Derailments and In-Service Failures

Equipment-caused train derailments can range from 100 to 150occurrencesper year [3]. Not only are derailments costly, ranging from $25,000 to $250,000 an hour depending on the derailment site, they are also dangerous for both people and the surrounding area. High-risk derailments can cause environmental contamination and will require extensive cleanup. Derailments are the most often heard cases of train failure. However, if following the transportation definition, risk can be thought of as the product of harm and probability. While in-service failures (ISFs) generally have shorter, less costly delays, they occur more frequently than derailments [4].

ISFs take place when the conductor is alerted of an immediate-action-required fault. This urgency prompts the conductor to halt the train in order to receive maintenance or replacement of the defective components. Granted that an ISF is less disastrous than a derailment, ISFs can cause secondary effects that will contribute to their impact. These secondary effects include reactionary delay to other trains in the route or network of the ISF's transit. Class I railroads have reported over 23,000 equipment caused ISFs in a year, often in response to reactive wayside detectors [4].

1.3 Wayside Condition Monitoring Systems

As an attempt to decrease freight train accidents, wayside condition monitoring systems were developed. Wayside monitoring systems are characterized by the same principle data acquisition method. These systems collect and analyze data obtained from bearings rolling over the detection system. If bearing conditions diverge from the predetermined threshold of a healthy bearing, the conductor is alerted so that appropriate actions can be taken.

1.3.1 Trackside Acoustic Detection System (TADS™)

The Transportation Technology Center Inc. (TTCI) developed TADSTM™ to monitor bearing health through acoustic signatures. TADS™ utilizes microphones to detect severe, high-risk defects in bearings as the train passes through the wayside system. These high-risk defects are termed "growlers" due to the low frequency the large spalled area (over 90% of the component raceway) produces. This system is an example of a reactive wayside detector, as it specializes in diagnosing end-of-life bearings. While TADS™ has a high proficiency in recognizing end-of-life bearings, not all severe defects are detectable through their algorithm and small or initiating defects will not be perceived [5]. As of March 2017, only 19 TADS™ are in operation nationwide, meaning that many freight cars can go through their entire service life without encountering one of these systems [6].

Figure 4. Photograph of a TADS™ site[6]

1.3.2 RailBAM®

In contrast with TADS™, RailBAM® is a bearing acoustic monitoring system sensitive enough to identify defects initiating on bearing components. This wayside acoustic detector has developed a reliable process for distinguishing severe and developing bearing defects. RailBAM®, shown in Figure 5, can process 200 wagons passing through the system at speeds greater than 50 km/h (30 mph) in less than 10 minutes [7].Native to southern Australia, only 20 RailBAM® detectors are in operation, causing the same predicament as TADS™ of neglecting railcars not passing through the system's routes. [6].

Figure 5. Photograph of a RailBAM® system

1.3.3 Hot-Box Detector (HBD)

Hot-Box Detectors (HBDs) work through a series of infrared sensors that scan bearings, wheels, and brakes as the rail cars pass over the detectors, as shown in Figure 6. If the operating bearing temperatures obtained through the HBD are greater than 76.7°C (138.06°F) above ambient or greater than 35°C (65°F) above the temperature of the bearing that shares the same axle, the train operator will be alerted. HBDs are placed approximately 40 km (25 miles) apart along the track. Over 6,000 detectors can be found across North American railroads, making these detectors the most common form of wayside condition monitoring system in the U.S. Even with the abundance of HBDs, there are still major problems encountered while analyzing this system.

A tapered roller bearing can overheat and may even burn off in just 1 to 3 minutes [6]. Assuming a maximum velocity of 129 km/h (80 mph), it would take a railcar approximately 20 minutes to reach the next HBD. This time interval between detectors gives rise to the possibility of overheated bearing failure. Conversely, at decreased speeds or while awaiting inspection, a bearing can cool down to normal temperatures making it difficult for the operator to properly assess bearing health. HBDs are stationary and have scanning ranges that are predetermined through calculated bearing dimensions for a specific class. As mentioned previously, bearing dimensions, both diameter and width, are subject to change with the bearing class. Varying bearing dimensions cause relative change in the position of the bearing on the axle. This causes the HBD measured temperatures to be inconsistent from actual bearing operation temperatures. Several studies have commented on the unreliability of HBD temperature readings through data acquired from laboratory and field tests [9][10][11].

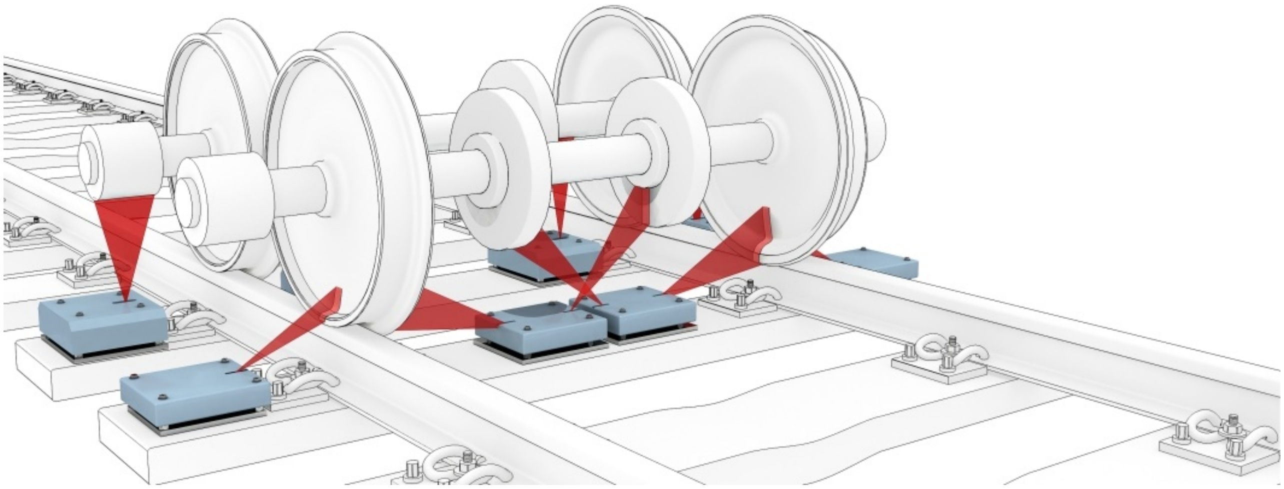

Figure 6. Example of a Hot-Box-Detector (HBD) site[8]

1.4 Onboard Condition Monitoring Systems

The short latency period between fault detection and failure occurrence in bearings creates concern in the use of wayside condition monitoring systems. Onboard fault detection methods were developed to achieve real-time condition monitoring. Onboard monitoring reduces costly reactive maintenance and improves safe transit by providing instant data of rolling stock health. These systems are meant to detect defect initiation and monitor progression to allow proactive maintenance schedules to be developed in order to decrease waste caused by preventative and reactive actions.

1.4.1 SMART-BOLT™

In the late 1900's Carnegie Mellon Research Institute (CMRI) developed a thermal sensor bolt for the continuous monitoring of bearing temperatures. This onboard monitoring system is designed to replace one of the bolts located at the end cap of the bearing, securing itself onto the axle. The location of the bolt was determined in order to minimize the variability of temperature gradients throughout the bearing caused by heating and cooling effects on the contact surface [12].SMART-BOLT™ consists of a battery, thermal-mechanical sensor, piston, and a transmitter. The transmitter is designed to alert the conductor once the bearing reaches the preset alarm temperature of 121°C (250°F). To facilitate inspection, the piston releases an antenna for quick identification of the overheated bearing. However, this antenna requires an authorized party to reset as the thermal actuator locks into place once it has been activated.

Although the normal operating temperature of a bearing is typically 81°C (178°F), bearing temperature trending is a common phenomenon occurring in defect-free bearings that exhibit end-of-life temperatures [13]. The locking mechanism of SMART-BOLT™ prevents continuous monitoring of the bearing in false positive cases. These interruptions make it difficult to obtain a reliable profile of the bearing condition, which would aid in creating proactive maintenance schedules.

1.4.2 Wireless Sensor Node

Wireless sensor nodes (WSN), such as the one developed by IONX shown in Figure 7, provide continuous real-time bearing temperature data to the locomotive engineer. WSNs contain Central Monitoring Units (CMU) which record both the bearing and the current ambient temperature [14]. WSNs use various algorithms to create a trend analysis of the bearing temperatures and provide early warning of possible failure. The CMU transmits this data via satellite or cellular network to the engineer for warranted action.

Figure 7. Field installation of a Wireless Sensor Node

1.4.3 Timken Guardian™ Bearing

The Timken Guardian™ Bearing is composed of a radio transmitter, microprocessor, power supply, and sensors placed within the bearing. These sensors monitor bearing conditions such as wheel rotational speed, temperature, and vibration, then proceed to transmit the data wirelessly through radio frequencies sent by the transmitter. The data can be sent either to a receiver on the railcar or store it in an off-site computer for future analysis. Once the receiver has been alerted to a possible defect, the bearing must be disassembled for a thorough inspection to be performed. Being one of the leading forms of bearing health monitoring, Timken Guardian™ Bearings are high-priced. These systems require the purchase of an entire bearing and can cause delays during disassembly and inspection if spare bearings are not available.

1.5 Purpose

Over the past 30 years, the U.S. railroad industry has invested in automated condition-monitoring technology (ACMT). Most wayside and onboard monitoring systems are reactive in nature, alerting only of imminent failure. This technology does very little in preventing ISFs given that immediate action is generally required at the notification of one of these systems. Still, the systems that provide continuous data to alert of onset bearing failure cannot provide remaining service life models. This lack of understanding in spall progression patterns often leads to premature maintenance and removal of tapered roller bearings.

The University Transportation Center for Railway Safety (UTCRS) research group at the University of Texas Rio Grande Valley (UTRGV) has developed a proactive bearing condition monitoring system which can reliably detect bearing defect initiation. The onboard condition monitoring system can continuously assess bearing health and provide accurate, real-time data. The reliability of this system has been validated through several laboratory and field tests at UTRGV and the Transportation Technology Center, Inc. (TTCI).

This system, Smart Adapter™, developed by UTCRS can measure temperature and vibration signatures of a bearing. Smart Adapter™ uses the root-mean-square (RMS) value of the bearing's acceleration to assess health and approximate spall size if a defect is found to be present. Then, an analysis of the frequency domain of the acquired vibration signature serves to locate the defect component location. The size estimated through the RMS value can then be used to predict the residual life of the bearing.

This thesis will focus on the development of a proactive and cost-efficient maintenance cycle for railcar tapered roller bearings using data acquired by Smart Adapter™. The data presented in this thesis can assist in eliminating costly delays and ISFs by proposing spall progression trends of bearing components most prone to deterioration. These trends will be used to provide remaining service life models of railroad rolling stock.

CHAPTER II

EXPERIMENTAL SETUP

The data presented in this thesis was acquired from experiments performed on dynamic bearing testers designed and manufactured by the University Transportation Center for Railway Safety (UTCRS). The testers are housed in the engineering labs at the University of Texas Rio Grande Valley (UTRGV). The four-bearing tester (4BT) can run four class K, F, E, or G bearings simultaneously, while the single-bearing tester (SBT) can accommodate one class K, F, E, or G bearing at a time. The data collected for this study was obtained from laboratory experiments in which only class K and class F bearings were tested. These specific bearing classes were chosen because they are the most widely used in freight rail transportation in the United States and Canada. Moreover, class F and K bearings use the same exact cone (inner ring) assemblies which allows for these components to be interchangeable.

2.1 Bearing Assembly

Class F and class K bearings are fabricated using AISI 8620 steel and the tapered rollers are case-hardened. The main components in these two bearing classes have the same dimensions, with the exception of the outer ring (cup) and the spacer ring. Due to class F cups having a larger width, the spacer ring that separates the cones must also be larger than that used in class K bearings. This causes minor changes in the bearing assembly with respect to the bearing grease lubrication and total weight.

2.1.1 Measurements

Every inner ring (cone) selected requires cage lift, cage shake, and roller spacing measurements to be taken. Cage shake and cage lift are performed with a dial indicator and serve to measure the lateral and vertical motions of the roller cage with respect to the cone. A setup of these measurements can be observed in Figure 8. Roller spacing measurements are carried out by inserting a feeler gauge in the space between the roller and the cage rib. These measurements are used to minimize the possibility of roller skew (misalignment) due to abnormal spacing in the cages holding the rollers against the inner ring. Maximum and minimum lateral measurements of the bearing assembly are also taken with a desired range of 0.023in to 0.028 in. Laterals help determine if the correct spacer ring has been selected. The spacer ring helps keep the bearings spinning parallel to the axle. Otherwise, like the rollers, the bearings might roll skewed, preventing optimum rolling speeds.

Figure 8. Cage measurement set-up: cage lift (left), cage shake (right)

2.1.2 Lubrication

The near-frictionless rotation experienced by tapered roller bearings is partly attributed to the lubrication it contains. Following the Association of American Railroad (AAR) standards, the bearings are filled with grease in the quantities and regions specified in Table 2. Class K bearings have a dimensional width of 22.9 cm (9 in) while class F bearings have approximately a 30.5 cm (12 in) width. While the cone assemblies are the same, the difference between these two classes of bearings is the spacer ring used. The width of a class K bearing spacer ring is approximately 1.46 to 1.48 cm (0.575 to 0.583 in). Whereas the spacer ring width for a class F bearing is between 3.68 and 3.94 cm (1.45 to 1.55 in). Due to the region of the cup (outer ring) between the two cone assemblies being noticeably smaller in class K bearings, no lubrication is applied to this spacer region for class K bearings.

Table 2. Lubrication (grease)application measurements for class K and class F bearings

Bearing Class	Total Grease [L] / [oz]	Spacer Region Grease [L] / [oz]	Cone Assembly Grease [L] / [oz]
F	0.6506 / 22	0.2662 / 9	0.3845 / 13
K	0.3845 / 13	N/A	0.3845 / 13

Once the bearing has been properly lubricated, it is secured with a grease seal and placed on a scale to measure the total weight. Depending on bearing class the weight can vary from 29.5 kg (65 lb) to 36.3 kg (80 lb). Additional weight can be caused by the cage type used within the bearing cone (inner ring) assemblies. Polyamide cages are significantly lighter than their counterpart steel cages.

2.2 Four-Bearing Tester (4BT)

The four-bearing tester is powered by a 22.4 kW (30 hp) variable speed motor that is controlled via a variable frequency drive (VFD). Through a pulley and its adapter, the motor creates axle rotational speeds that can be translated into track speeds, as shown in Table 3. A hydraulic cylinder is used to apply loads of up to 150% of full load, with full load corresponding to a force of 153 kN (34.4 kips) per class F or K bearing. Notice in Figure 9, which depicts the four-bearing tester, the hydraulic cylinder applies vertical load directly on bearing 2 (B2) and bearing 3 (B3). Therefore, a total of 306 kN (68.8 kips) are applied to the two middle bearings (153 kN or 34.4 kips per bearing) with the reaction forces also applying 153 kN (34.4 kips) on each of the outer bearings (B1 and B4). In order to replicate field service operating conditions, only data acquired from the two middle bearings (B2 and B3), which are top loaded, were used in this study.

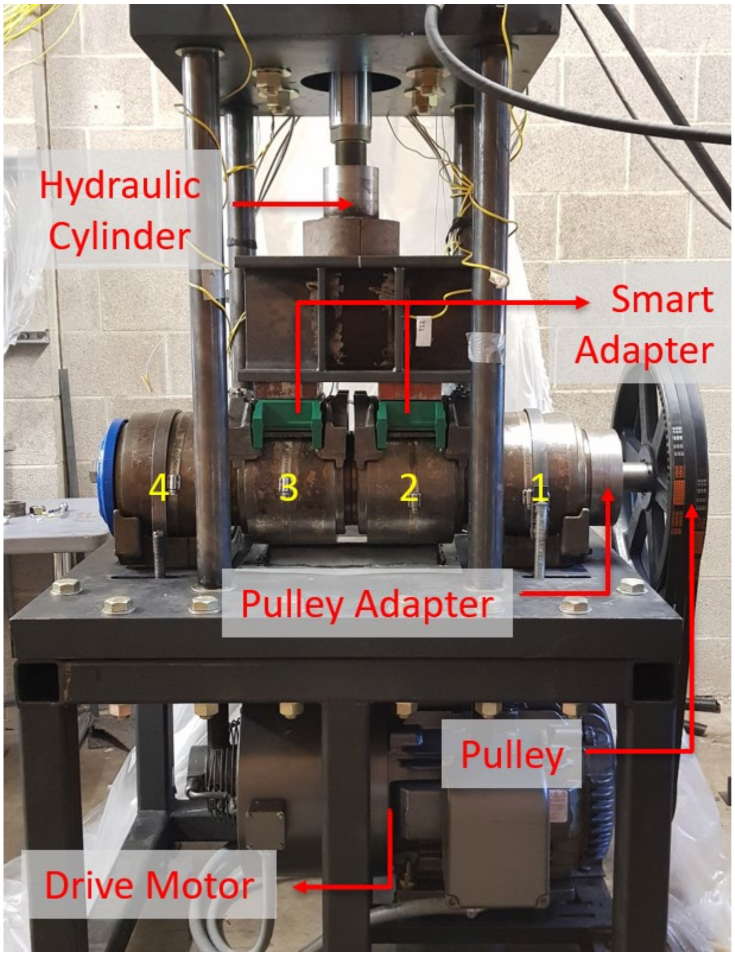

Figure 9. Four-Bearing Tester (4BT)

Table 3. Axle to Track Speed Conversions

Axle Speed [rpm]	Track Speed [mph] / [km/h]
280	30 / 48
327	35 / 56
373	40 / 64
420	45 / 72
467	50 / 80
498	53 / 85
514	55 / 89
560	60 / 97
618	66 / 106
699	75 / 121
799	85 / 137

For this study, it was necessary to track and record the temperature and vibration signatures of the test bearings. To do so, the steel adapters were machined to accept two 70g accelerometers placed in the outboard SmartAdapter^{TM} (SA) and mote (M) locations, along with one 500g accelerometer placed in the outboard radial (R) location. To monitor the bearing operational temperature, the adapter was outfitted with two bayonet thermocouples placed in the middle of each raceway, and one regular K-type thermocouple that was held tightly against the middle of the outer ring (cup) utilizing a hose clamp. The modified adapter displaying the accelerometer (right) and thermocouple (left) locations is pictured in Figure 10.

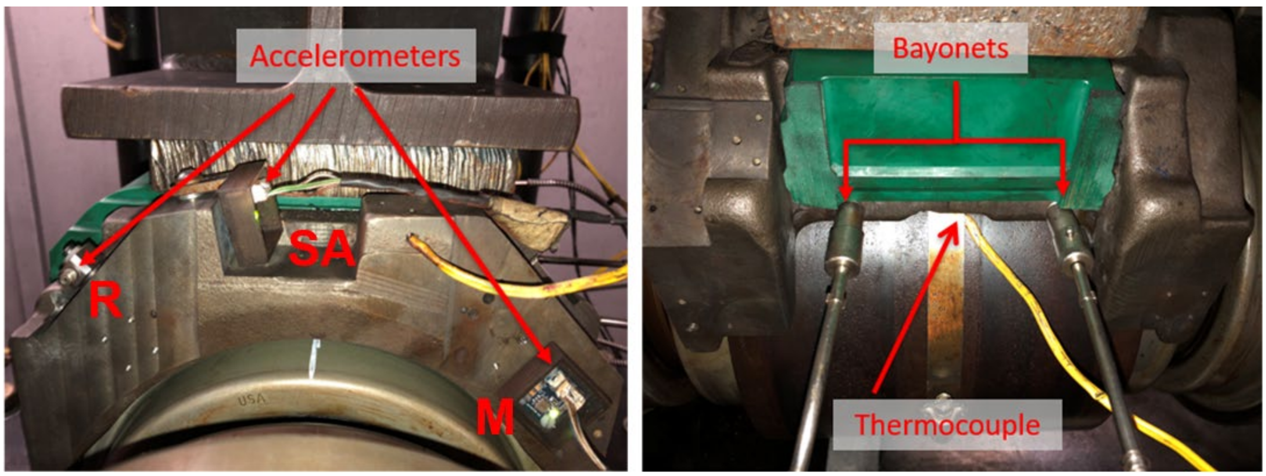

Figure 10. Modified 4BT adapter showing vibration sensors (left) and temperature sensors (right)

Two industrial size fans were used to simulate the convective cooling that bearings in field service experience due to crosswind passing over the bearings while the train is in motion. The fans generate average airflow speeds of approximately 6 m/s (13.4 mph). A schematic of the fan and 4BT layout is presented in Figure 11. The specially constructed, temperature-controlled environmental chamber which houses the 4BT is equipped with a commercial freezing unit with a cooling capacity of 7.6 kW (10.2 hp). The chamber can simulate a wide range of ambient temperatures with lows of -40°C (-40°F) and highs of as much as 65.6°C (150°F). This allows the four-bearing tester to mimic the extreme ambient conditions that might be experienced during service across routes in various seasons and climates.

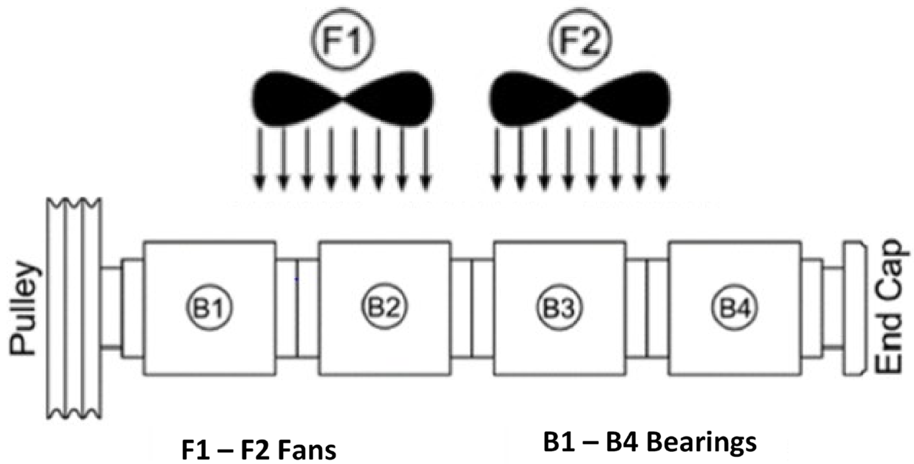

Figure 11. Top view of four-bearing tester (4BT)

2.3 Single-Bearing Tester (SBT)

The single-bearing tester (SBT) is designed to hold a single class F or class K bearing on a specially fabricated 4140 steel axle. The main objective of the cantilever design of the single bearing tester, which can be seen in Figure 12, is to accurately reproduce field service operating conditions. Similar to the 4BT, the SBT is equipped with a 22.4 kW (30 hp) variable speed motor, capable of providing the operational speeds listed in Table 3. A hydraulic cylinder, identical to that of the 4BT, is used to apply vertical loads. However, unlike the four-bearing tester, the single bearing tester can also apply lateral and impact forces which can be used to mimic the field service conditions of a railcar experiencing hunting and/or wheel impacts, or passing over bad rail track segments. The SBT can provide maximum lateral loads of up to 22 kN (5 kips) and maximum vertical loads of up to 222 kN (50 kips).

Another feature of the cantilever design of the SBT is that it allows for easy installation and removal of the test bearing. Thus, the single-bearing tester was primarily utilized to run experiments on bearings having spalls with areas larger than 6.45 cm^2 (1 in^2). These larger spalls require frequent disassembly and visual inspection to be carried out to closely track defect progression.

Aside from two industrial size fans supplying convective cooling, as those used on the four-bearing tester, the SBT employs a specially designed cooling system fabricated by the UTCRS research team. The setup allows for chilled water to run over the pillow blocks which house the support bearings. The purpose of incorporating this system is to prevent the tester's support bearings from overheating during an experiment.

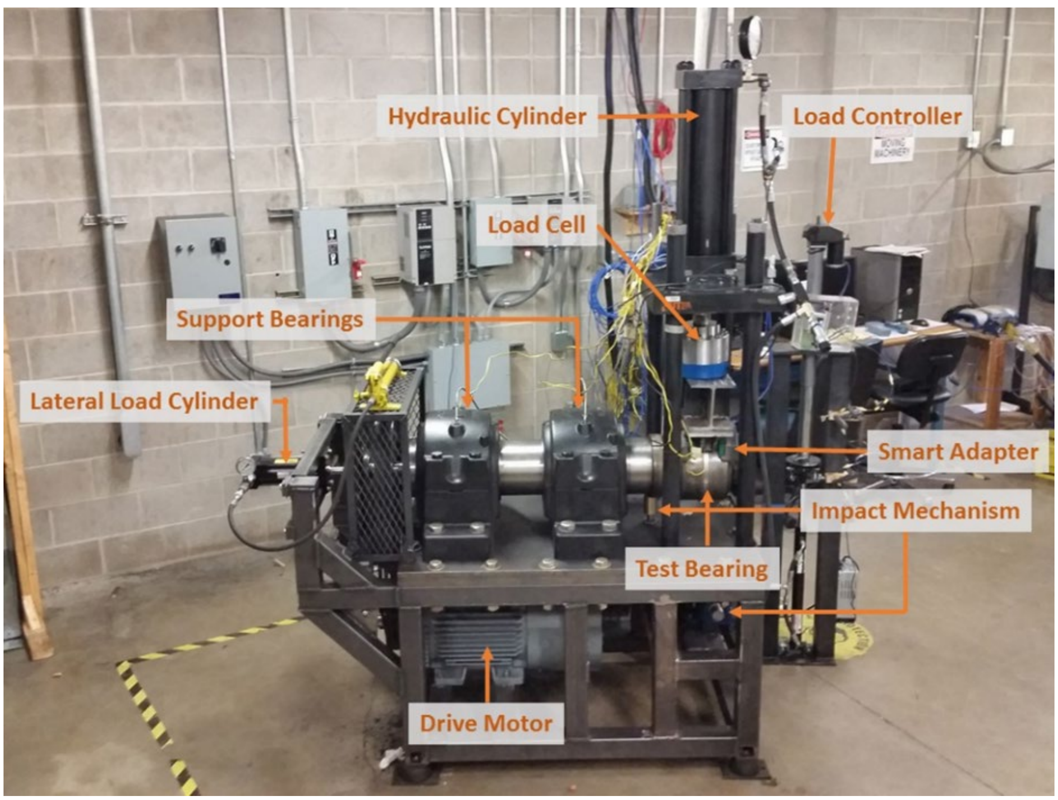

Figure 12. Single bearing tester (SBT)

Again, the steel adapter was machined to accept vibration and temperature sensors. For vibration monitoring, four 70g accelerometers were placed in the SmartAdapter™ (SA) and mode (M) locations at both the inboard and outboard sides of the bearing, along with one 500g accelerometer in the radial (R) location on the outboard side. Temperature data was acquired through two inboard and two outboard bayonet thermocouples affixed to the bearing adapter. Additionally, seven K-type thermocouples were held via a hose clamp around the circumference of the bearing. The bearing thermocouple locations are shown in Figure 13.

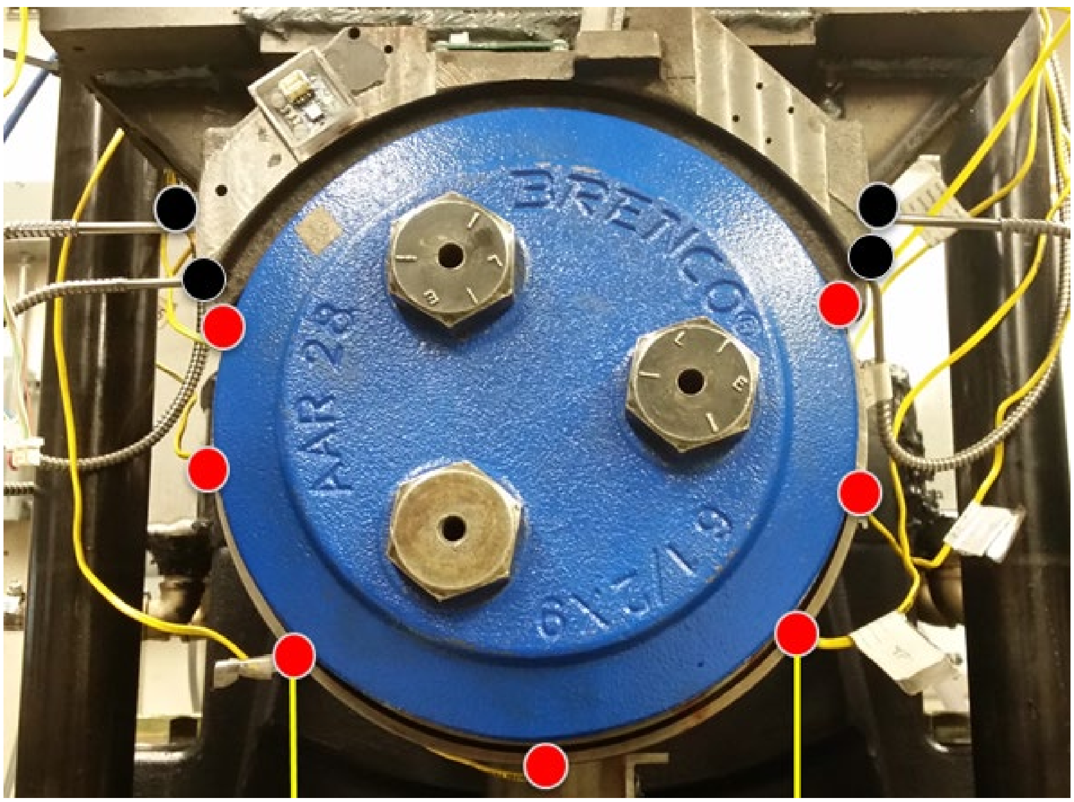

Figure 13. Single bearing tester thermocouple locations: bayonets represented by black dots, K-type thermocouples represented by red dots

2.4 Data Acquisition

LabVIEW™ was used to program of a National Instruments (NI)cDAQ-9174 data acquisition (DAQ) system utilized to log vibration and temperature signatures received from the test bearings. Temperature data was obtained from the thermocouples every 20 seconds for half a second at a sampling rate of 128 Hz. K-type thermocouples were connected to the NI 9213 temperature card of the DAQ to collect the bearing temperature profiles. Vibration signature acquisition was performed through accelerometers connected to a combination of 8-channel NI 9239, NI USB-6008, and NI 9234 cards via 10 - 32 coaxial jacks and BNC connections. The accelerometers collected vibration data every ten minutes for 16 seconds with a sampling rate of 5,120 Hz.

CHAPTER III

DEFECT DETECTION, SPALL MAPPING, AND SPALL GROWTH

The University Transportation Center for Railway Safety (UTCRS) research team has worked towards acquiring bearing vibration and temperature profiles for over twelve years now. The data presented for defective bearings pertains to two primary sources: service-life tested bearings and bearings removed from field service. Service life testing was performed with defect-free bearings that contained at least one subsurface (≤ 600 μm) inclusion after being ultrasonically scanned[15]. All service life testing of defect-free bearings was carried out exclusively on the four-bearing tester (4BT) until a defect (i.e., spall) developed. As a result, the mileage leading to the development of a spall in a bearing undergoing service life testing was closely tracked.

The majority of the bearings removed from service were pulled from freight railcars due to defective wheelsets, and upon visual inspection were found to have relatively small inner ring (cone) or outer ring(cup) defects (less than 6.45 cm^2 or 1in^2). It is important to note that defects with areas below 6.45 cm^2 (1in^2) are seldom, if at all, detected by current wayside condition monitoring detectors. The removed bearings did not trigger any wayside detectors and there was no notion of an existing defect, thus the mileage leading to the development of the spall cannot be determined.

While the distance traveled leading to the formation of the spall can be accurately tracked for bearings that underwent service-life testing in the laboratory, it is impossible to obtain the pre-spall mileage for bearings that have been removed from field service. The initiation of a spall is greatly influenced by the material purity and quality and the manufacturing process used. Each component has material impurities and subsurface inclusions that are unique to the component. Thus, a large variance in the spall initiation mileage of a tapered roller bearing component is expected. Consequently, to ensure the appropriateness of both data sets, the mileage prior to the initiation of a surface defect was not factored in the model development. Hence, the developed models are functions of the distance traveled after a component has developed a spall (defect), where the initial spall formation is taken as the zero-distance reference point.

3.1 Defect Detection

The defect detection algorithm developed by Gonzalez [16] can detect, with 95% accuracy, the onset and propagation of tapered-roller bearing raceway defects. The algorithm is activated when operating speeds are above 65 km/h (40 mph) or when the bearing's operating temperature surpasses 93°C (200°F). Once the accelerometer is triggered, the algorithm will go through three levels of analysis to provide information pertaining to the bearing condition including the presence of any spalls (defects), defect classification, and approximate defect size.

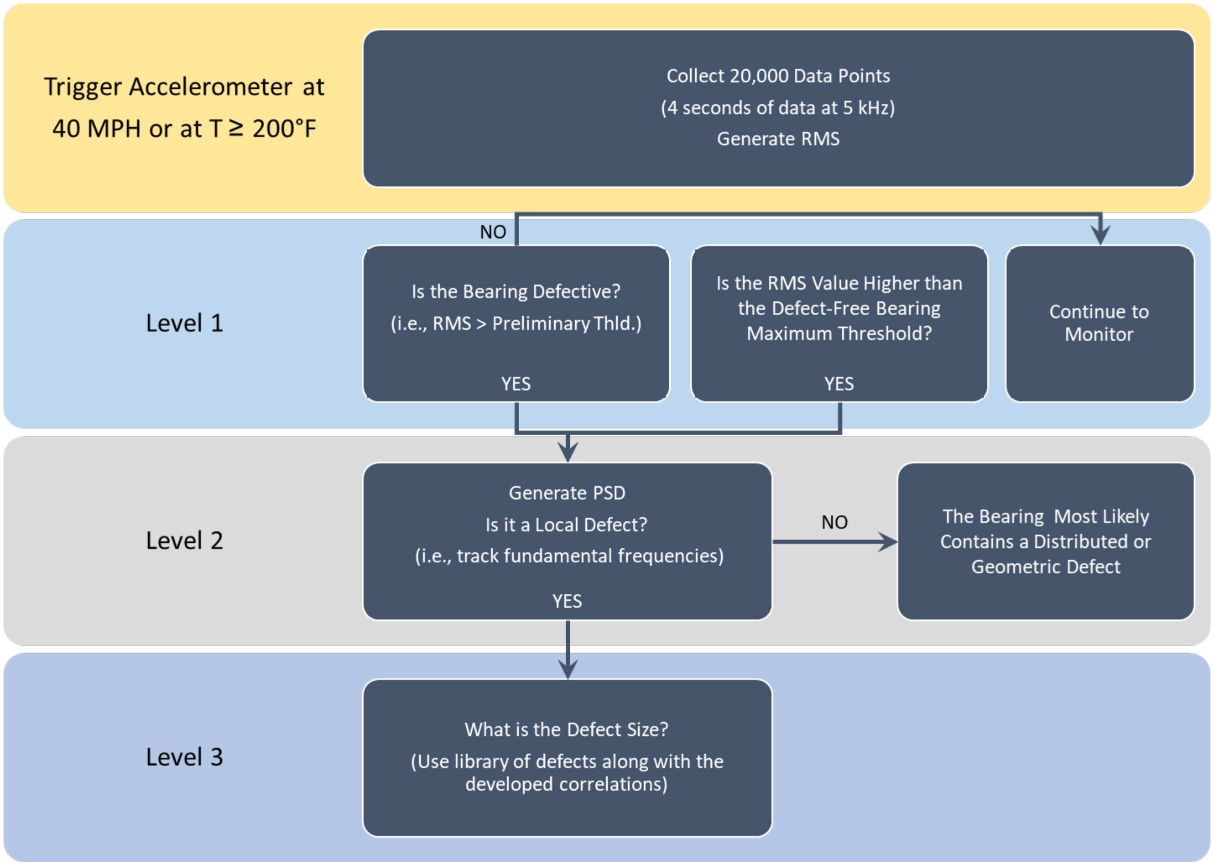

Figure 14. Defect detection algorithm flowchart [16]

Level 1 analysis is the first step in the three-tier algorithm and serves to identify whether the bearing is healthy (defect-free) or defective. Through years of data collected from bearing testing and vibration monitoring, a margin for healthy bearing vibration signatures was determined. This threshold establishes the maximum possible vibration levels within a defect-free bearing at simulated train speeds ranging from 48 km/h (30 mph) to 137 km/h (85 mph). If the vibration levels within a bearing, as measured by the root-mean-square (RMS) values of the acquired vibration data are higher than the maximum threshold at a specific speed, the bearing is identified as defective and the algorithm proceeds to Level 2 analysis.

Categorization of the defect type present in a tapered-roller bearing is done in Level 2 analysis. As mentioned earlier, there are three defect classifications: localized, geometric, and distributed. Level 2 is mainly a frequency-domain analysis where power spectral density (PSD) plots are generated. These PSD plots are then analyzed to obtain the fundamental bearing frequencies and their harmonics. The railroad tapered roller bearing fundamental frequencies are described in detail in reference [16]. In Level 2 analysis, these fundamental rotational frequencies are tracked and used to find the corresponding defect frequencies for the outer ring (cup), inner ring (cone), and roller, as well as their harmonics. A localized defect in one of these components manifests as high peaks at the corresponding defect frequency and its harmonics in a PSD plot, thus, alerting of a localized defect in that component. If a localized defect is identified in Level 2 analysis, the algorithm will proceed to Level 3 analysis. However, if none of the three defect frequencies (cup, cone or roller) and their corresponding harmonics display dominant behavior, yet RMS value calculated in Level 1 analysis is higher than the maximum threshold for health bearings, then the defect is either a geometric or a distributed defect. In his case, the algorithm does not proceed to Level 3 analysis.

Level 3 analysis provides an estimate of the localized defect area(size) for the defective bearing component identified in Level 2 analysis. Level 3 analysis relies on previously developed vibration data correlations to obtain good estimates (generally within 10%) of the defect area. The defect size correlations for the outer ring (cup) and inner ring (cone) produced by Gonzales are shown in Figure 15 and Figure 16, respectively. These defect size correlations were later enhanced by Montalvo [17]. A correlation for the rollers was not developed due to the infrequency with which a roller defect occurs in rail service unaided by the spalling of its surrounding components.

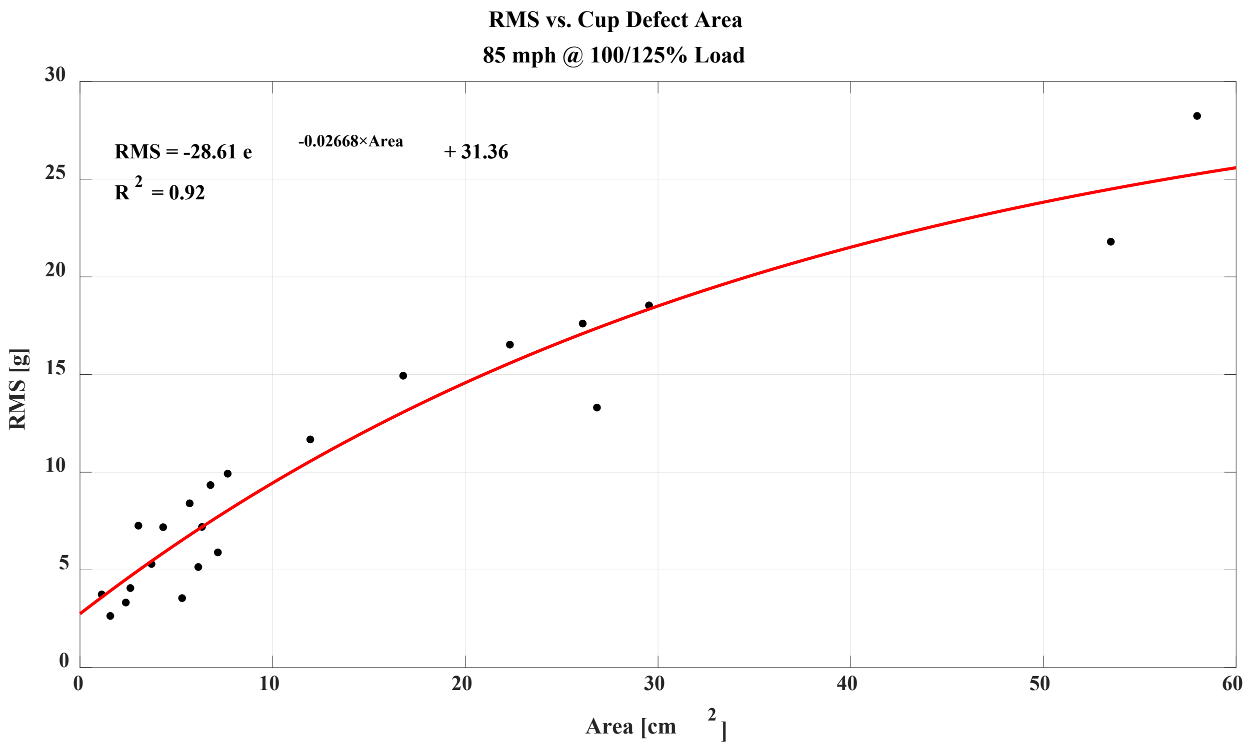

Figure 15. RMS - Cup defect size correlation at 137 km/h (85 mph) and full load[16]

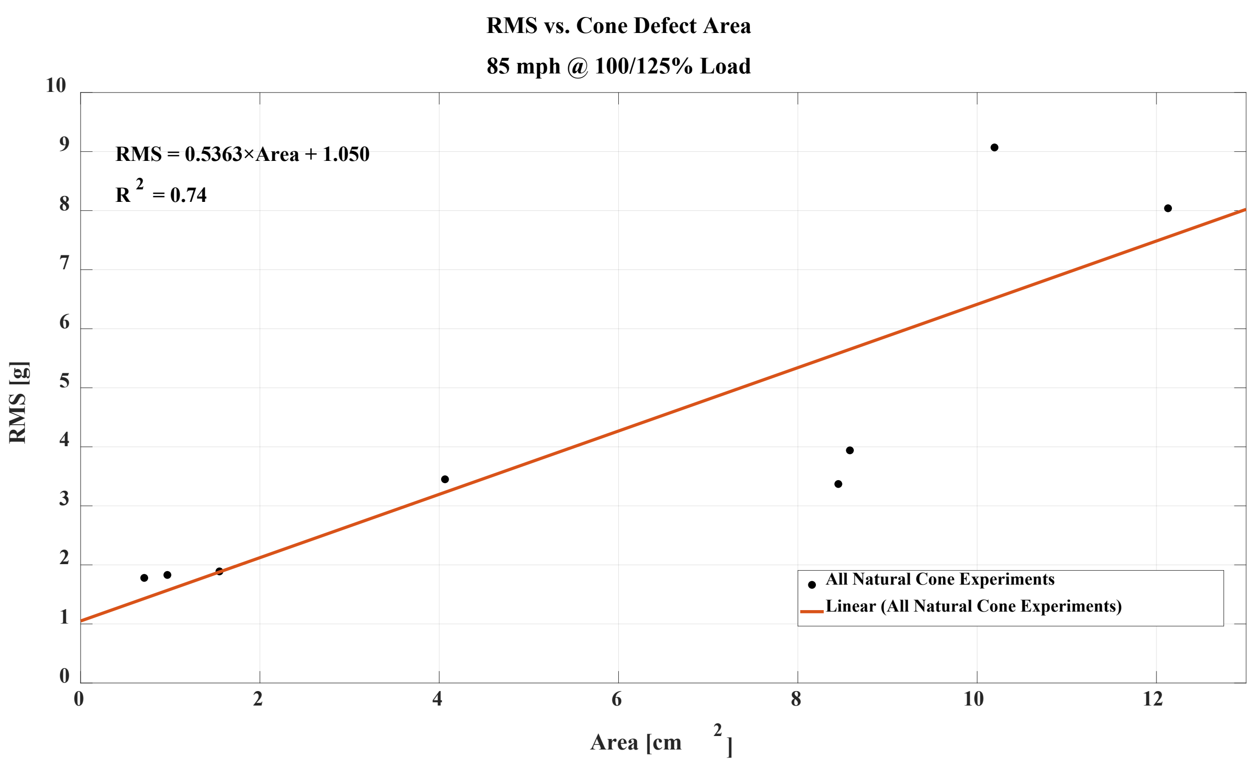

Figure 16. RMS - Cone defect size correlation at 137 km/h (85 mph) and full load[16]

3.2 Spall Casting

Once the vibration monitoring algorithm alerts of signatures above the threshold for a healthy bearing, the experiment is stopped, the bearing is disassembled, and each component is visually inspected. If a defect has developed or a spall has propagated, the area is cleaned thoroughly and surrounded with sealant tape (capable of withstanding a maximum temperature of 204°C or 400°F). After the sealant tape creates a mold around the defect area, a molten bismuth alloy with a melting temperature of 80°C (176°F) is poured into the sealant tape frame enclosing the spall. The casting process is depicted in Figure 17. These casts help keep a reliable record of the spall areas and their progression when the bearing is reassembled and pressed onto the test axle for further defect propagation.

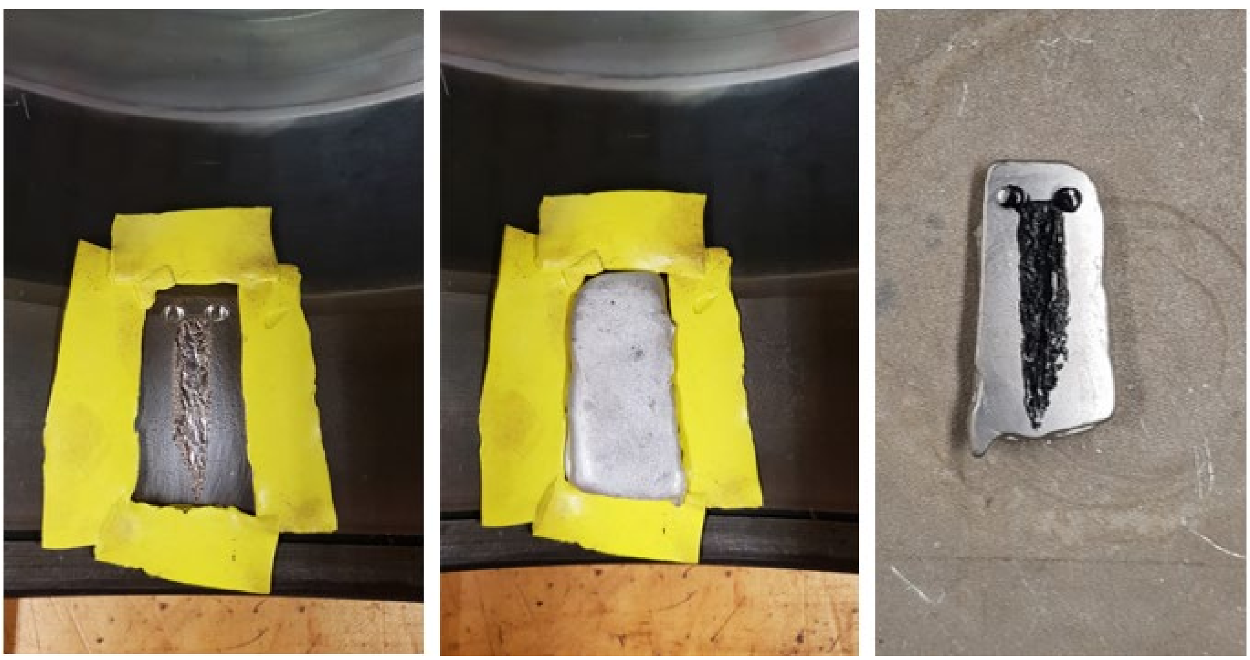

Figure 17. Casting procedure using sealant and bismuth tape

The spalled portion of the cast is painted to mark a contrast between the defect area and the surrounding mold. A photograph is taken of the painted cast alongside a ruler and uploaded to MatLab® where a code was written to create a monochromatic image of the photograph. This post-processed image is then imported to Image Pro-Plus® to perform digital analysis of the defect region. Using the ruler in the image as reference, Image Pro-Plus® uses optical techniques to report accurate defect area parameters in an Excel sheet. The Excel sheet provided by Image Pro-Plus® is transferred to a spreadsheet where test experiment data is compiled. The spreadsheet provides comprehensive data regarding mileage, vibration signatures, spall area, and defect growth.

3.3 Spall Growth Patterns

Defect area and mileage data were analyzed in order to observe the spall growth behaviors. Variables such as raceway and component location as well as defect size were studied. Several patterns in the development of a spall have been observed, especially in relation to the size and location parameters. While the orientation of the subsurface inclusion might be of consequence to spall progression patterns, the bearings removed field service do not have a documented history of being ultrasonically scanned and therefore, the existence and orientation of any surface inclusions cannot be verified. Therefore, subsurface inclusion orientation was not one of the factors considered in this study.

Spall raceway locations can be categorized into three underlying types: edge, center, and full-width[18].The most common raceway spalling location is the edge, shown in Figure 18 (left). Although edge spalls can occur on either border of the raceway, inner ring (cone) defects will generally develop on the smaller diameter rim while many outer ring (cup) defects will develop in the larger diameter segment of the raceway. This edge defect pattern is attributed to stress “flow lines” crowded together in the rib zone. Center spalls, as the one depicted in Figure 18 (center), are less typical than edge defects on account of the rib-roller stresses experienced on the raceway leading to edge spalling prominence [19]. A spall will initially propagate along the width of the raceway until both roller/rib contact borders are reached, exemplified by the full-width spall in Figure 18 (right). Once the edges are reached, the spall will expand circumferentially along the component raceway.

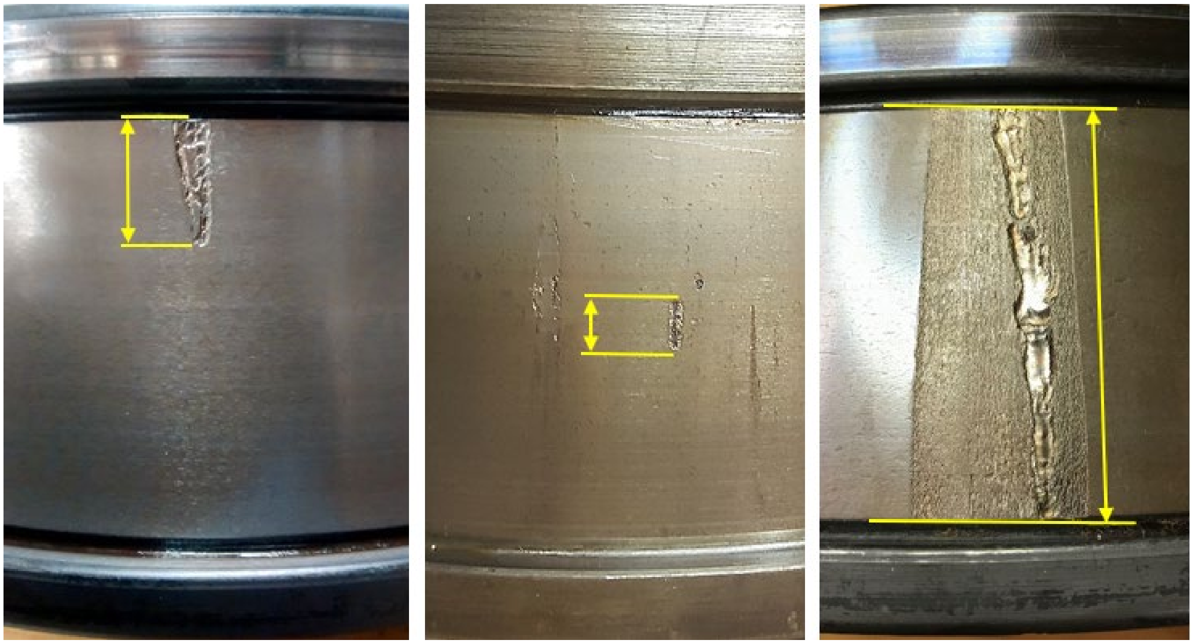

Figure 18. Spall regions depicted in inner rings: edge (left), center (center), full-width (right)

Whereas the growth patterns mentioned are attributed to both inner ring (cone) and outer ring (cup) components, there are differences in the propagation models of these elements that should be noted. The width of an outer ring raceway is approximately 5.513 cm (2.170 in), making it larger than the 4.984 cm (1.962 in) corresponding to an inner ring raceway. However, the most prominent difference between these two components is their loading cycles. As previously mentioned, the outer ring (cup) is a static component causing the loaded region to experience constant stress. The inner ring (cone) cycles in and out of the loaded zone creating cyclic stresses in the component.

3.3.1 Inner Ring (Cone)

A noticeable trend is observed when correlating the defect area with total distance traveled, shown in Figure 19. The dash-dotted line across 6.45 cm^2 (1 in^2) marks a threshold for two distinct growth rates of inner ring defects. Findings demonstrate that cone spalls with areas larger than that of the stated threshold (6.45 cm^2 or 1 in^2) will produce faster defect progression rates than those below the threshold [20]. In addition to the accelerated deterioration, larger spall areas display less variation (R^2=0.86) in their growth pattern compared to the more dispersed (R^2=0.38), below-threshold, counterpart.

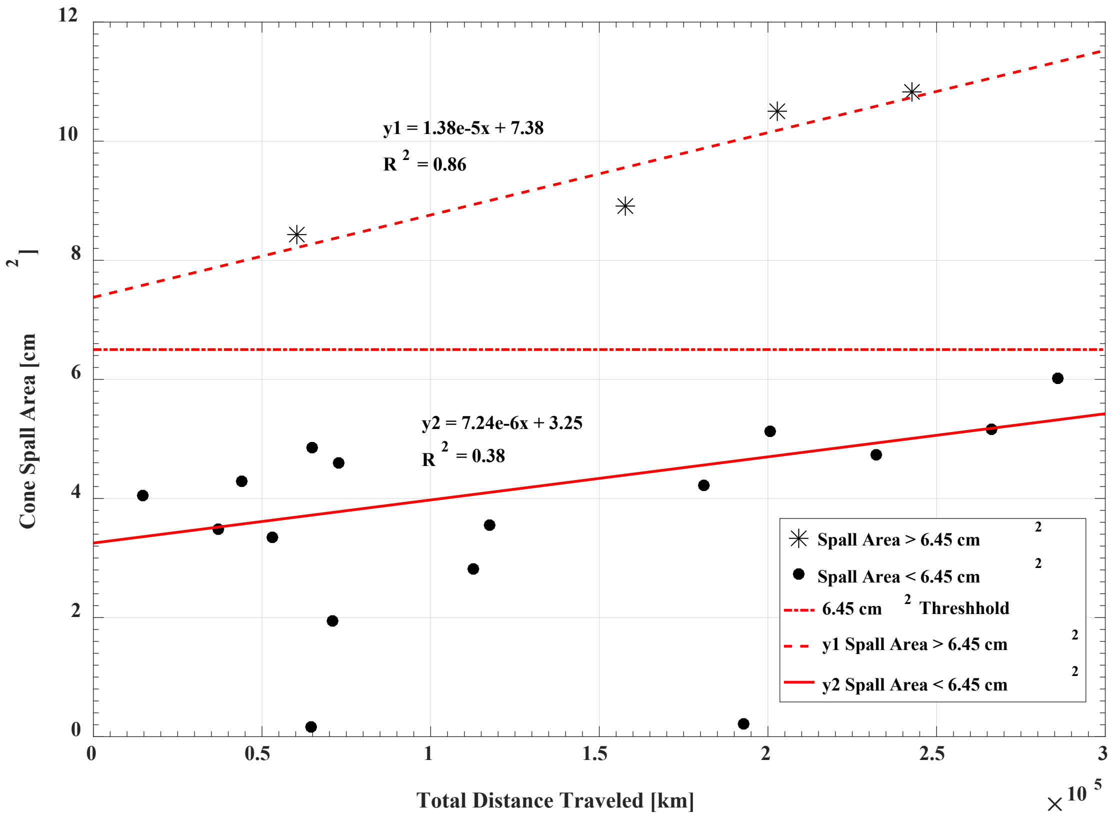

Figure 19. Cone spall size vs total distance traveled [20]

The variation in the deterioration models above and below the designated threshold can be attributed to the growth pattern of tapered-roller bearing defects. As stated earlier, surface defects will initially grow throughout the width of the raceway due to the roller contact area stresses. Despite the typical patterned growth of a developing spall, the raceway allows for some lateral expansion to occur as the defect spreads across the width. Once the entire raceway width has been covered by a spall, the only remaining growth is in the lateral direction. The onedirectional growth experienced by larger, above-threshold, defects covering the raceway width supports the decreased divergence seen in the regression analysis.

3.3.2 Outer Ring (Cup)

Like the cone spall growth data, the outer ring defect propagation model, shown in Figure 20, presents the spall area as a function of the total distance traveled. This graph exhibits two distinct growth rates between spall areas above and below 12.9 cm^2 (2 in^2). Defect areas larger than the threshold have a markedly steeper deterioration trend in addition to having a better fit (R^2=0.81). An explanation for the difference in slope and divergence of these two propagation patterns can be attained from the same logic used for the inner ring components. The spall will grow along the width of the raceway, with slight lateral dispersion. As the defect begins to reach the boundaries of the raceway it will decelerate growth. After the defect has spanned the entire width of the raceway, the spall can propagate laterally, unbound by rib contact.

Another interpretation for the two distinct defect growth rates and accelerated deterioration of larger defects can be attributed to larger spalls in the raceways allowing enough contact area for the roller to enter the defect depression. When passing over the defect cavity, the roller engages the spall shoulder creating lateral loads as opposed to those typically observed during the vertical contact stresses. The lateral loads experienced by larger spalls will increase the subsurface shear stress which can lead to faster growth rates.

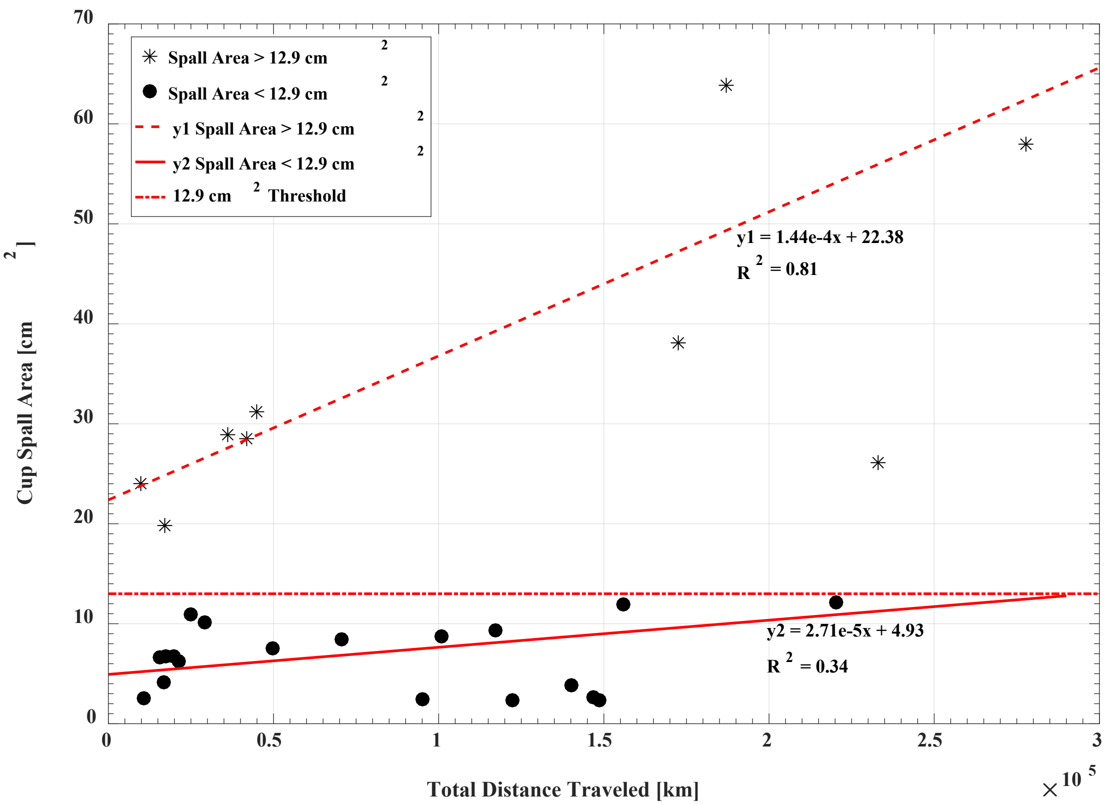

Figure 20. Cup spall size vs distance traveled [20]

In spite of the inner ring (cone) and outer ring (cup) having similar spall growth trends, the primary difference observed between Figure 19 and Figure 20 is the threshold area. This variation in the threshold area for these two models is attributed to the roller contact area in the components [20]. The cone, a convex surface to the roller, will experience approximately 7% smaller contact areas than the concave surface provided by the outer ring (cup) raceway. A visual representation of these geometries is provided in Figure 21. When calculating the Hertzian contact stress, a smaller contact area yields a larger depth of max shear stress as well as 10% higher maximum Hertzian contact stresses [21].

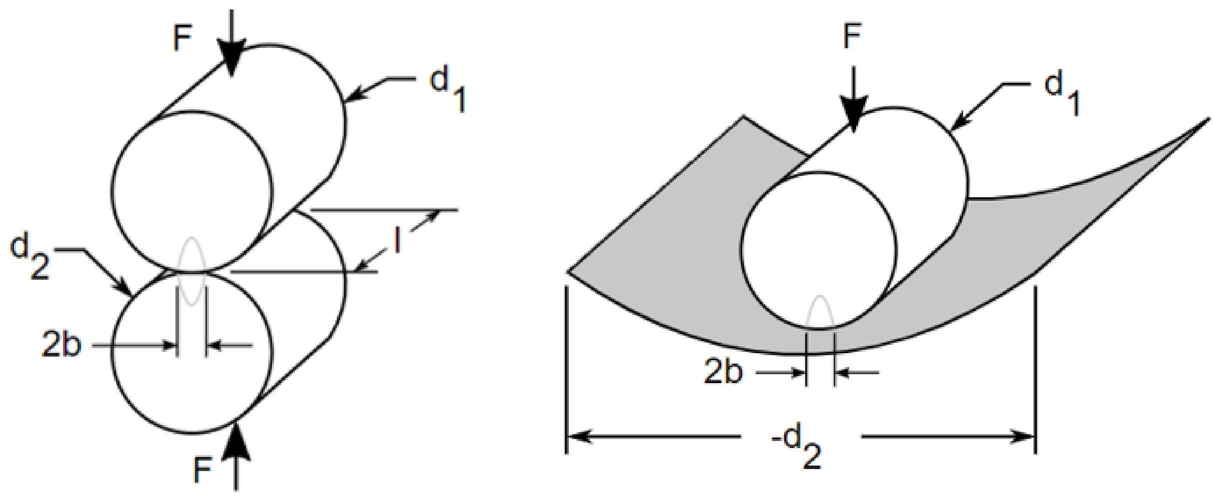

Figure 21. Contact area models: convex inner ring (left), concave outer ring (right)

CHAPTER IV

RESULTS AND DISCUSSION

The residual life models developed for a defective tapered roller bearing component, along with demonstrations of their effectiveness, will be presented in this chapter. Outer ring (cup) and inner ring (cone) data utilized to create these models was obtained from experiments performed over the past ten years by the University Transportation Center for Railway Safety (UTCRS). To ensure reliable RMS data, vibration and temperature profiles were obtained from loading conditions of 100 – 125% and speeds ranging from 121 – 137 km/h (75 – 85 mph). RMS and temperature values displayed are the average of the readings taken from the last two experiment hours. For experiments performed on the four-bearing tester (4BT) readings from the SmartAdapter™ (SA) accelerometer were considered, while tests moved to the single bearing tester (SBT) had RMS readings averaged from the inboard and outboard SA locations.

4.1 RMS and Defect Area Correlation Models

Continued data acquisition allowed for the enhancement of the previously developed RMS versus defect area correlation models shown in Figure 15 and Figure 16. The cup defect area versus RMS regression analysis maintained an exponential trend while exhibiting an increase in R^2 to 0.93, shown in Figure 22. The largest difference was seen in the inner ring relation in Figure 23 which, while retaining its linear form, increased to an R^2 value of 0.94 once further population was accomplished. While the cup and cone trend lines maintained their original structure, the equations were slightly modified to conform the new data points obtained.

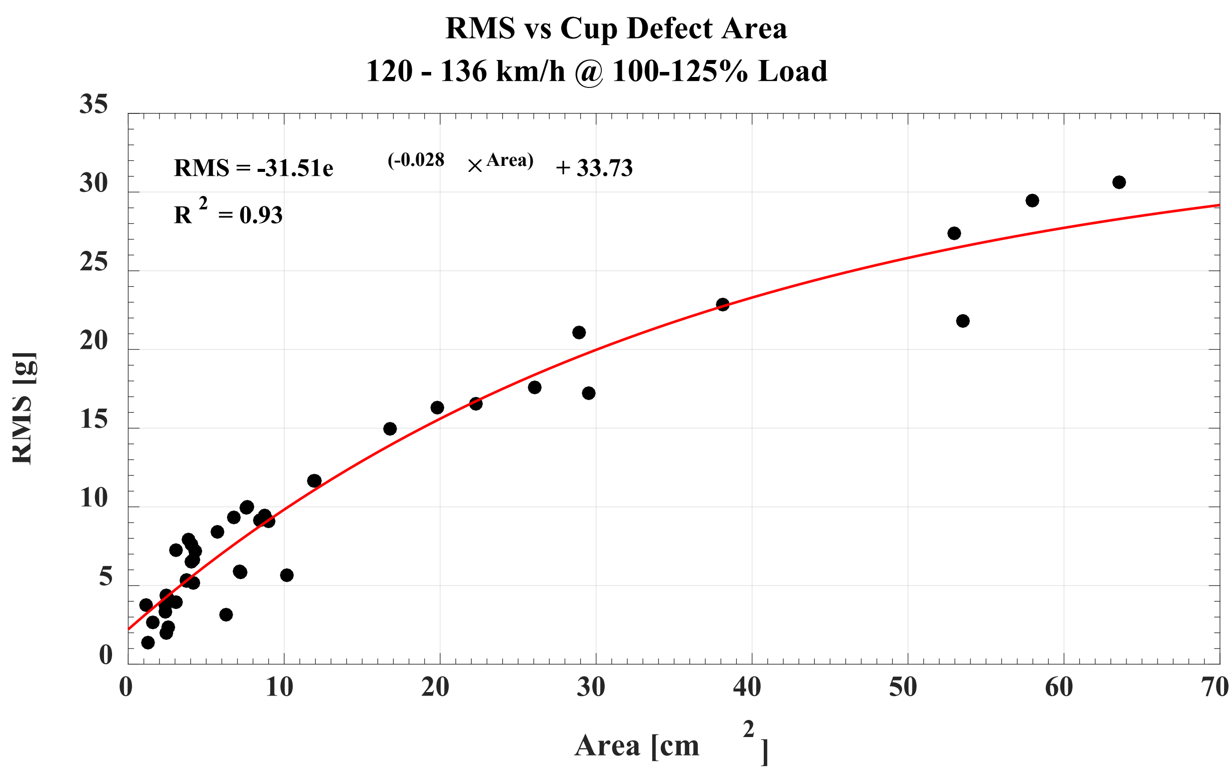

Figure 22. Improved regression analysis of RMS vs cup spall area

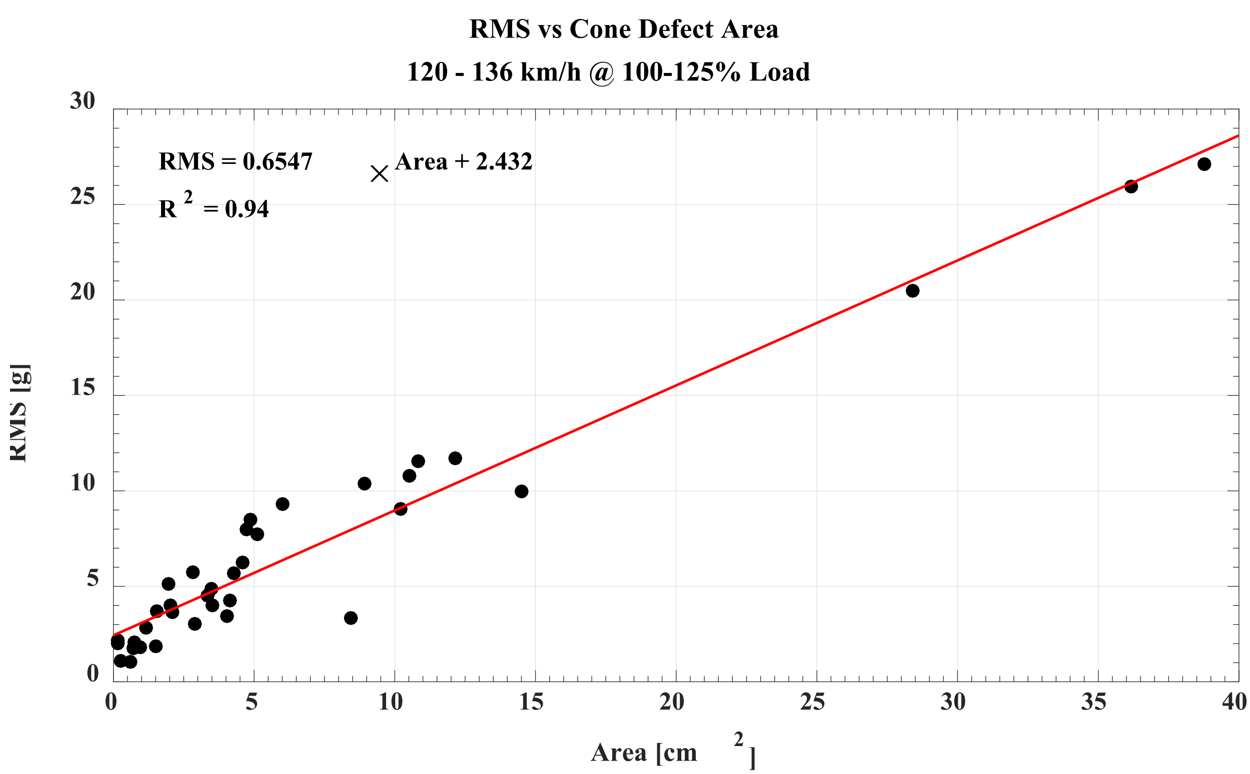

Figure 23. Improved regression analysis of RMS vs cone spall area

The revised regression analysis for component vibration signatures with respect to defect area, displayed in Figure 24 for outer rings and Figure 25 for inner rings, was standardized through the vibration levels shown in Table 4. These RMS ranges were decided upon through extensive experience in defect deterioration patterns observed through the experiments performed in UTCRS. The categorization was utilized to organize the regression analysis into four distinct levels depending on the RMS readings of the defective bearing component.

While the condition parameters in Table 4 apply to both inner rings and outer rings, it is important to note that the average defect area corresponding to the RMS ranges selected will vary for each component. Outer rings can allow for defects with average sizes of 13 cm^2 to give a yellow indication (monitor condition), whereas inner rings will pass onto a monitor condition (yellow indication) at an average spall area of 9 cm^2. The disparity in the average defect area between these two bearing component conditions only increases with the RMS values. For an RMS value of eight or less, the average defect areas of inner ring(cone) and outer ring (cup) components have a difference of 1 cm^2, which increases to 20 cm^2 by the time RMS values correspond to a red indication (RMS > 25).

Table 4. Catalogued condition parameters using RMS values

Average Defect Area [cm^2]		**RMS Value [g]**	**Condition /Indication**	**Residual Mileage [km] / [mi]**
Cup	**Cone**			
4	3	< 8	Good / Green	> 80k / 50k
13	9	8 – 17	Monitor / Yellow	40k – 80k / 25k – 50k
35	28	17 – 25	Warn / Orange	16k – 40k / 10k – 25k
58	38	> 25	Act / Red	< 16k / 10k

The average defect area variation in cup and cone components coincides with that seen in the spall area thresholds of Figure 19 and Figure 20.The threshold observed in the cone spall area versus mileage regression analysis shows that an inner ring spall will have an accelerated deterioration trend at a defect area lower than that of an outer ring. The accelerated propagation rate threshold in cones can explain the higher RMS values at lower defect sizes considering a faster deterioration will create increased vibration signatures. Another reason for the lower defect size in inner rings is the components motion behavior. It has been established that the bearing outer ring is a static component while the inner ring rotates with the axle. While both elements experience the rollers rotating and revolving along the raceway, complimentary cone rotation in and out of the loaded zone creates higher defect frequency (ω=167.8 Hz) than that seen in a stationary cup (ω=135.6 Hz). Cone rotation will also result in prolonged spall progression. Due to their cyclic loading, bearing inner rings will not encounter the constant stresses experienced by outer rings and thus will take longer to reach larger spall sizes. As a result, there is an observed scarcity in the cone vibration analysis for defect areas above 15 cm^2.

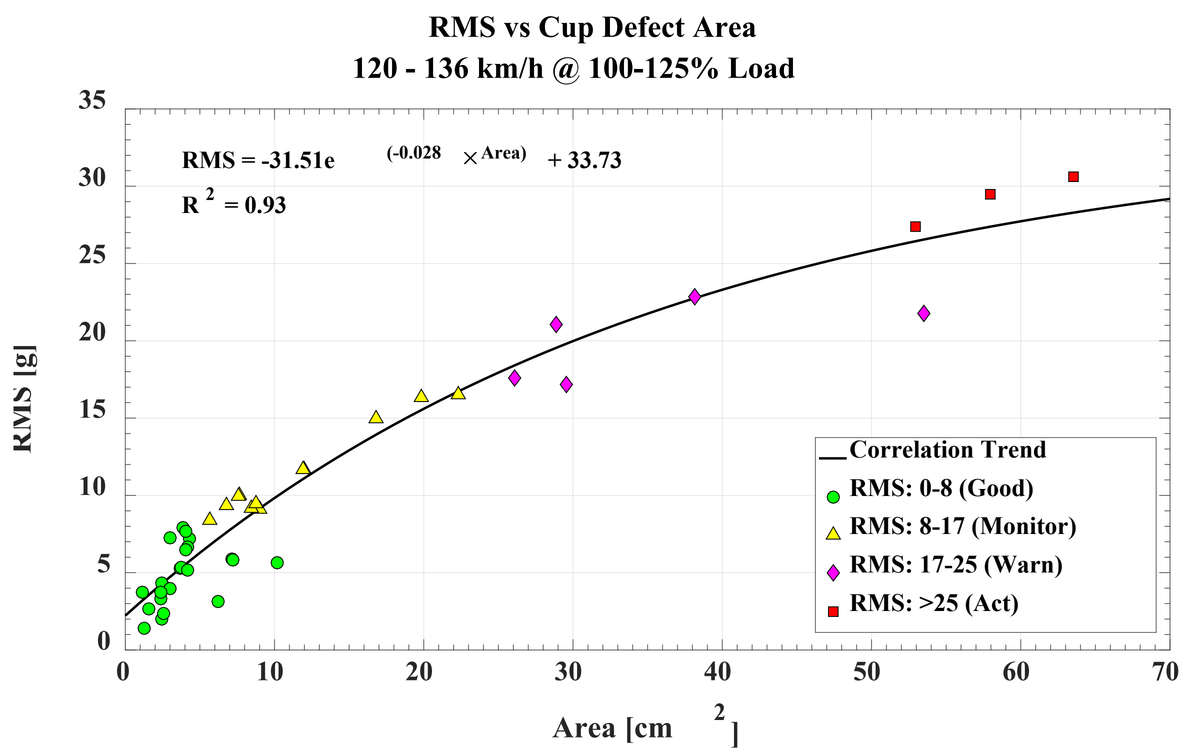

Figure 24. RMS vs cup spall area regression analysis with condition parameters

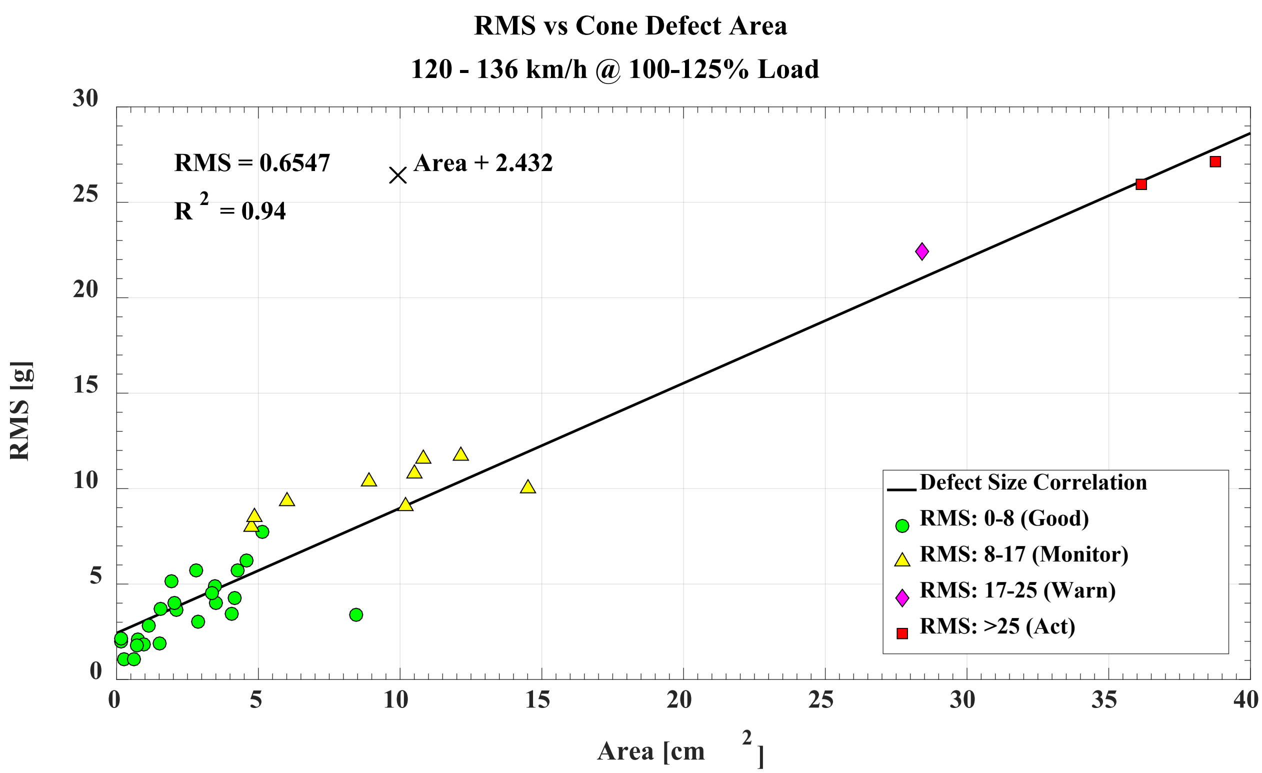

Figure 25.RMS vs cone spall area regression analysis with condition parameters

4.2 Spall Growth Rate Patterns

The mileage of each experiment was recorded and used to calculate the component spall area growth rate. Figure 26 and Figure 27 shows the area growth rate versus the defect area for cups and cones, respectively. Two trends were developed in both the outer ring (cup) and inner ring (cone) data gathered: an upper bound growth rate correlation (GR1) and a lower bound growth rate (GR2). It was necessary to produce two trends due to uncertainty in the amount and location of subsurface inclusions in each raceway. A raceway with several clustered subsurface inclusions near the surface of the raceway will have defects develop at a faster rate as opposed to a raceway with fewer or more dispersed subsurface inclusions. The GR1 equation is used to provide a worst-case scenario for estimating the residual life of a defective cup while assuming an abundance of subsurface inclusions. While GR2 serves as a lower bound equation that provides a baseline growth rate for its respective component.

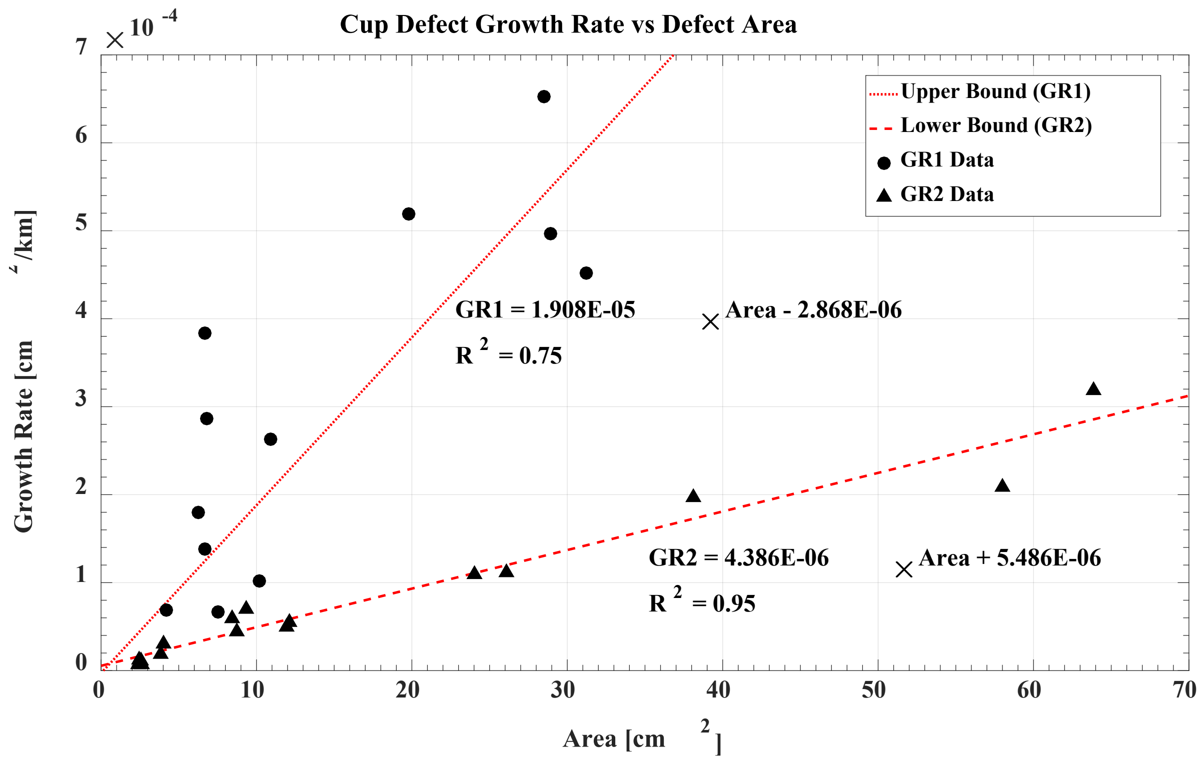

Figure 26. Cup spall area growth rate versus cup spall area

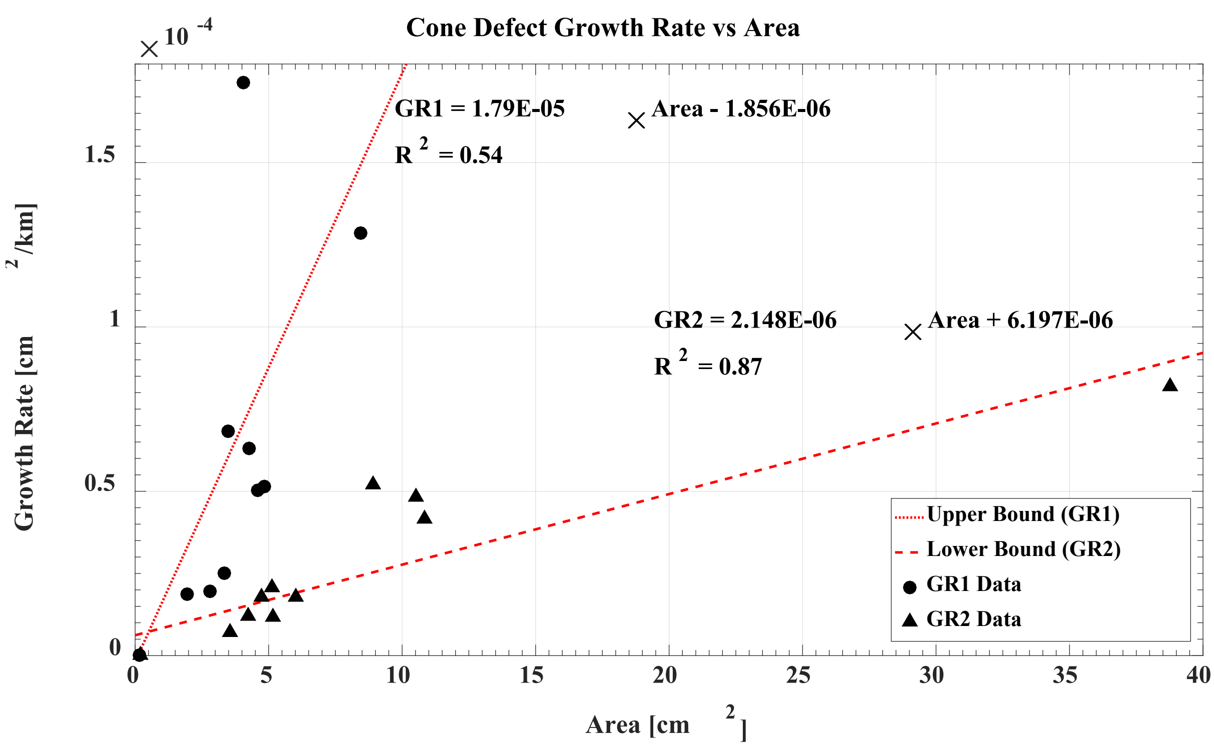

Figure 27. Cone spall area growth rate versus cone spall area

Observing the growth rate models, it is seen that the R^2 for both the inner ring and outer ring GR1 trend line is lower than that for the GR2. The scatter in the GR1 data points can be attributed to the variation in quantity and location of the material's subsurface inclusions. Location of subsurface inclusions is significant both in depth and in proximity to another. Material impurities conglomerated in a single area are likely to group and create an accelerated growth rate.

A correlation between RMS and defect growth rate was obtained using the equations provided by the RMS versus defect area and the defect growth rate versus defect area regression analysis models. The area variable in each growth rate trend was equated to the area variable in its respective component RMS regression line. These equations were used to form the RMS and defect growth rate relationships for cups and cones seen in Figure 28 and Figure 29, respectively. The upper bound (GR1) and lower bound (GR2) in these models are used to form a confine in which the calculated defect growth rate will fall in once the RMS value is known.

The outer ring trendlines seen in Figure 28 display natural logarithmic (ln) equations due to the exponential function found in the RMS versus defect area regression analysis. The growth rate confine formed between the GR1 and GR2 boundaries is initially limited and increases with the RMS as the exponential trendlines begin to diverge from each other. Since RMS increases as the defect area grows larger (seen in Figure 22 and Figure 23), it is appropriate to say that larger defects have a higher growth rate margin. Figure 29 displays the same GR1 and GR2 behavior for the inner rings with the exception of a linear function for both the upper and lower growth rate trendlines due to the cones linear trend seen in its RMS versus defect area plot (Figure 23).

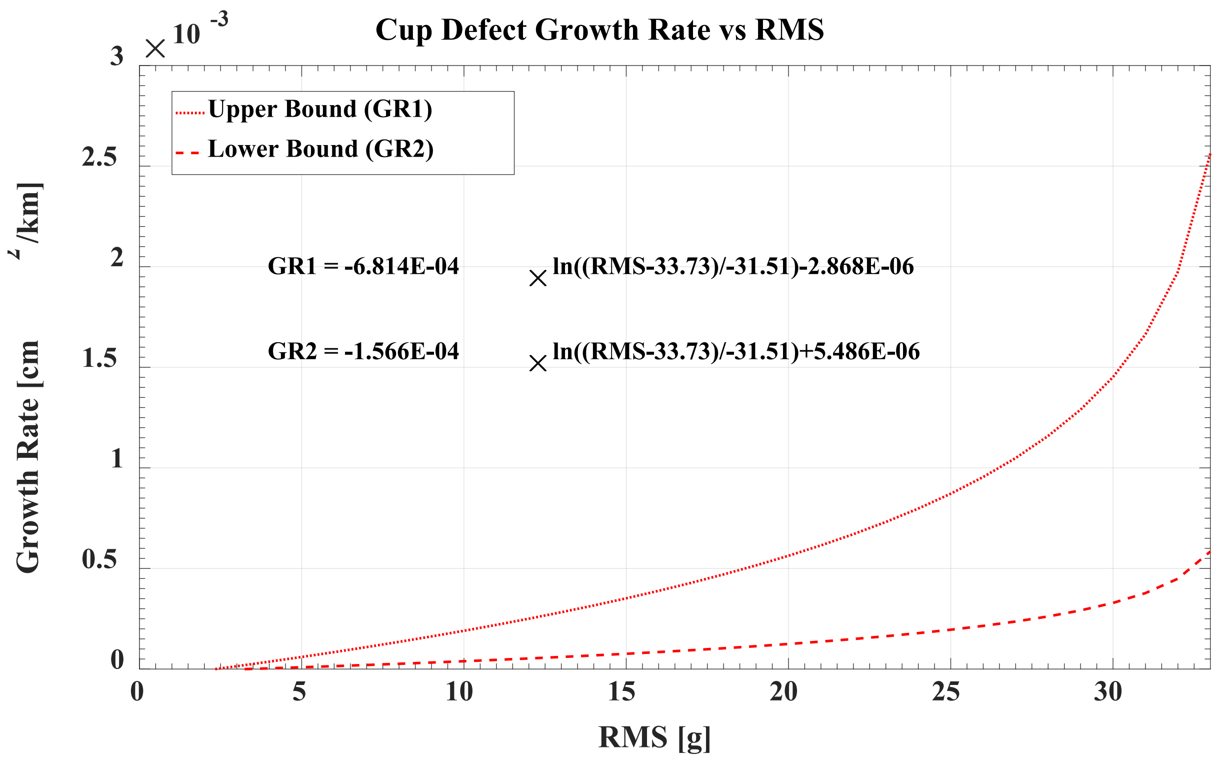

Figure 28. Cup spall area growth rate versus RMS

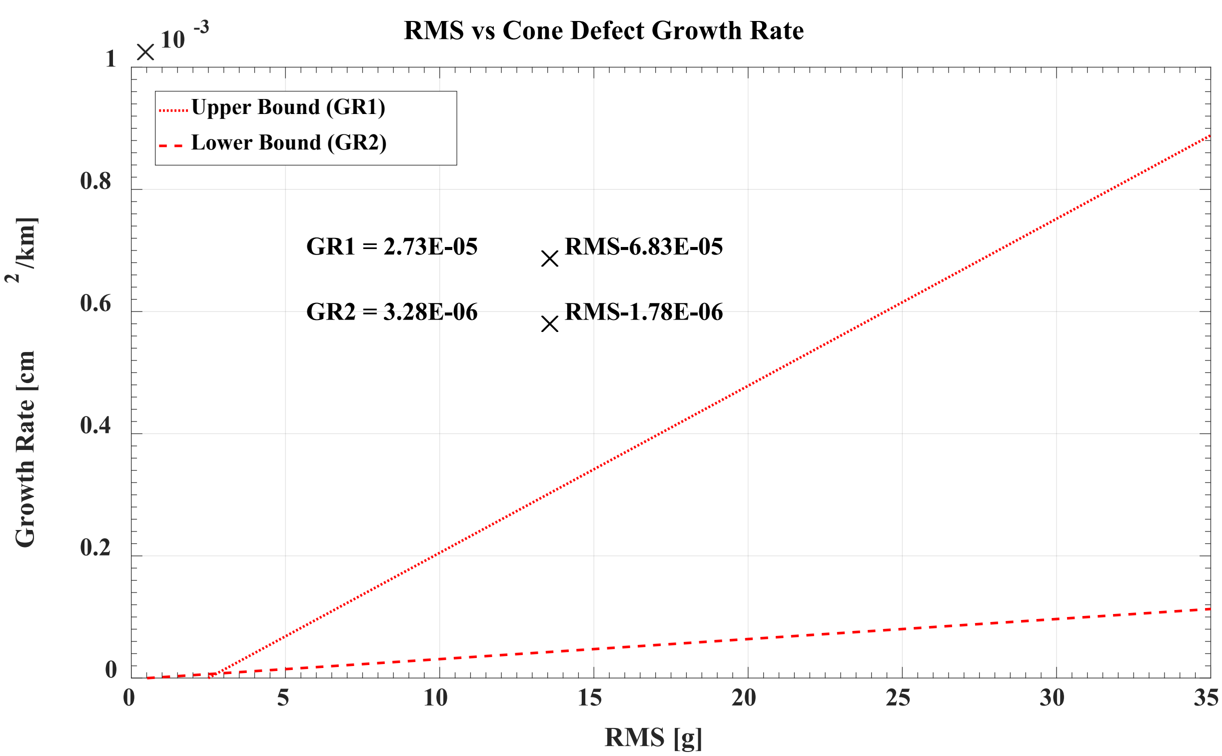

Figure 29. Cone spall area growth rate versus RMS

4.3 Laboratory Experiment

4.3.1 Laboratory Experiment 200: Cup Defect

Experiment 200 consisted of an outer ring (cup) with an initially pitted inboard raceway, shown in Figure 30 (left). The cup ran on the four-bearing tester (4BT), placing the pitted area under the maximum loaded region to simulate a worst-case scenario. The experiment ran a total of 81,600 km (50,700 miles) in which the pitted raceway developed a spall with an area of 9 cm^2 (1.4 in^2), shown in Figure 30 (right). The developed defect area corresponds to approximately 2.5% of the total area (367 cm^2) of a class K or class F outer ring raceway.

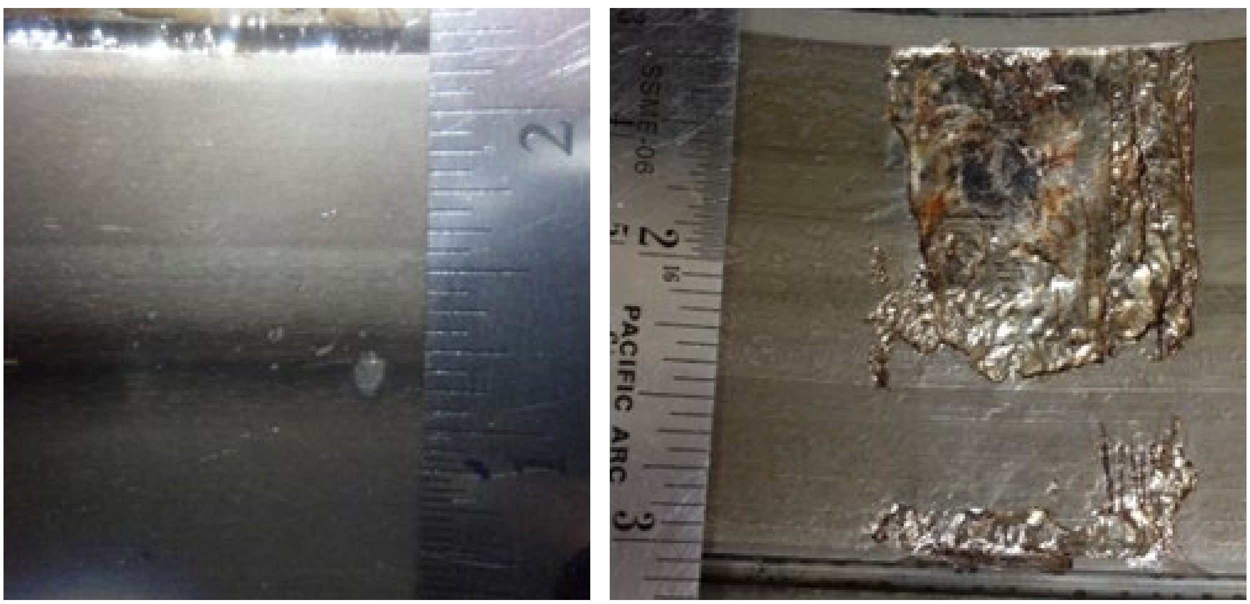

Figure 30. Experiment 200: Initial cup raceway (left) and final cup raceway (right)

Figure 31 displays the vibration and temperature profiles for B2 during Experiment 200, operated at full speed (137 km/hr) and 110% of full load conditions. The bearing was pulled out once it was deemed defective through the condition monitoring algorithm. The maximum threshold in the vibration and temperature profiles denote the highest value a healthy bearing will display under the given conditions. Therefore, any bearing operating with a signature above the maximum RMS threshold is expected to be defective and removed from the experiment in order to be inspected for defect propagation.

Averaging the last two hours of the SA accelerometer, an RMS of 9 g was found. The RMS was used to calculate a theoretical defect area using the equation found in the outer ring RMS versus defect area regression analysis (Figure 24). The calculated defect area of 8.8 cm^2, shown in Table 6, had a 98% accuracy to the actual. The RMS was also used to calculate the upper and lower growth rate boundaries for the defective outer ring. Using the GR1 and GR2 equations from the growth rate versus RMS plot the upper and lower bounds yielded values of 1.7E-04 cm^2/km and 0.4E-04 cm^2/km, respectively. The actual growth rate of 1.0E-04 cm^2/km fell well between the range provided by the regression analysis, as can be observed in Figure 32.

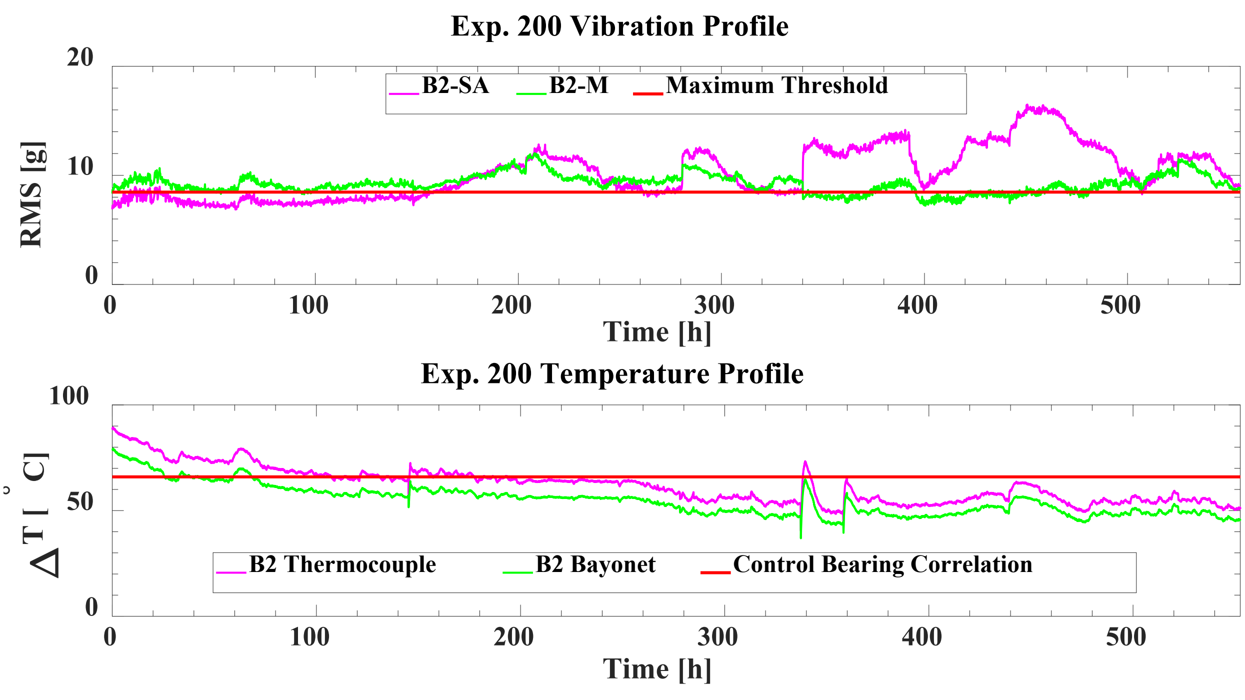

Figure 31. Vibration and temperature profiles for Experiment 200

Table 5. Average values for the final two hours of Experiment 200

Experiment 200 (Bearing 2 Cup Spall)			
Track Speed [km/h]/[mph]	Load [%]	ΔT [°C / °F]	RMS [g]
137 / 85	110	48 / 87	9

Table 6. Spall size and spall growth rate values for Experiment 200

RMS	**Defect Size [cm^2]**	**Calculated Defect Size [cm^2]**	**Accuracy [%]**
9	9	8.80	98
	Lower Bound Growth Rate [cm^2 / km] * 10^{-4}	**Actual Growth Rate [cm^2 / km] * 10^{-4}**	**Upper Bound Growth Rate [cm^2 / km] * 10^{-4}**
	0.4	1.0	1.7

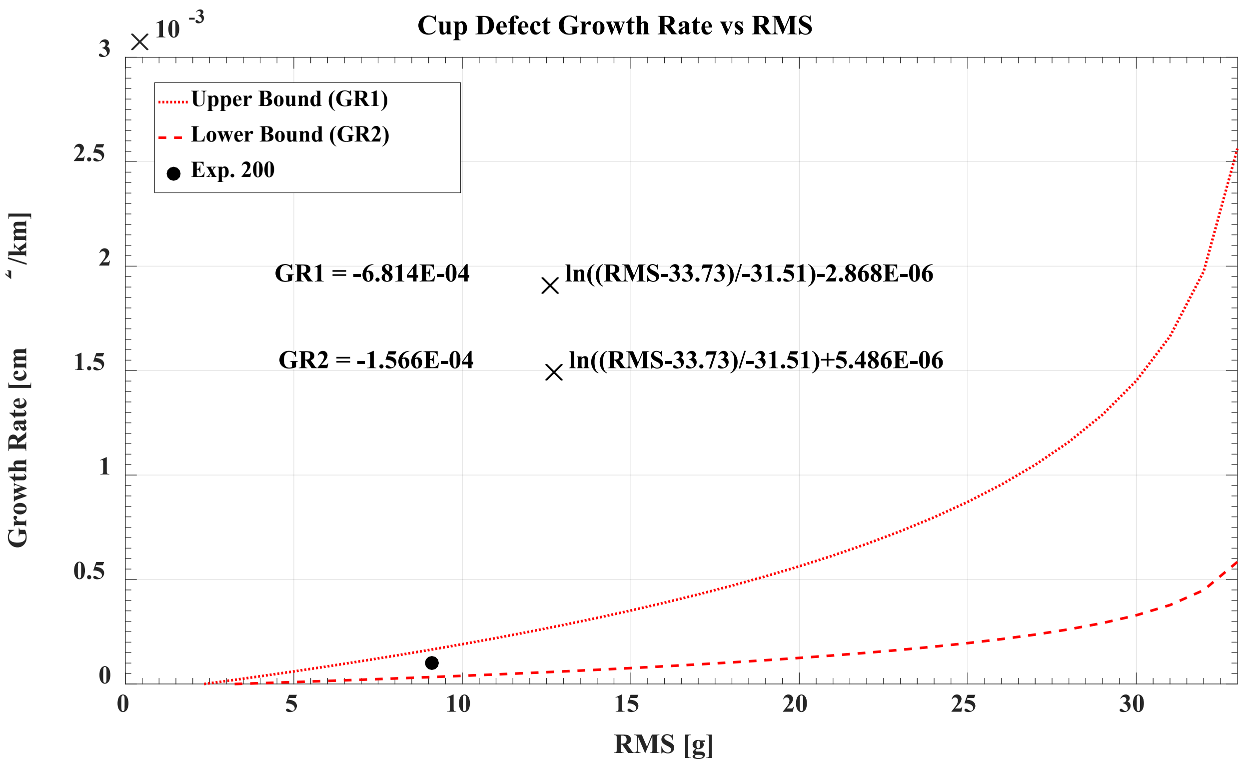

Figure 32. Experiment 200 settled in cup spall growth rate regression model

The average spall size corresponding to an outer ring (cup) red indication (act condition) is 58 cm^2, which accounts for 16% of the total 367 cm^2 for a single class K or class F outer ring raceway area. If the upper bound growth rate of 1.7E-04 cm^2/km is used to create a worst-case defect propagation scenario, it will take approximately 304,000 km (189,000 mi) for the spall to grow to a size where action will be required (red indication). This residual life prognostic allows for a conductor to have plenty of time to develop a proactive maintenance schedule which will minimize costly premature maintenance and stoppages.

4.3.2 Laboratory Experiment 184B: Cup Defect

An outer ring (cup) with an inboard spall area of 24 cm^2 (3.7 in^2), which had a previous vibration signature of 16 g (monitor condition), was placed in the B3 location of the four-bearing tester (4BT) for further defect propagation. As with Experiment 200, Experiment 184B had the defect location positioned directly under the maximum loaded region. After running a total of 47,000 km (29,000 mi), at full speed and full load conditions, the defect area grew to a size of 53 cm^2 (8.2 in^2), shown in Figure 33 (right). The post experiment defect warranted a red indication (act condition) due to its vibration signature giving an RMS of 27 g while encompassing 14% of one outer ring raceway area (367 cm^2).

Figure 33. Experiment 184B: Initial cup raceway (left) and final cup raceway (right)

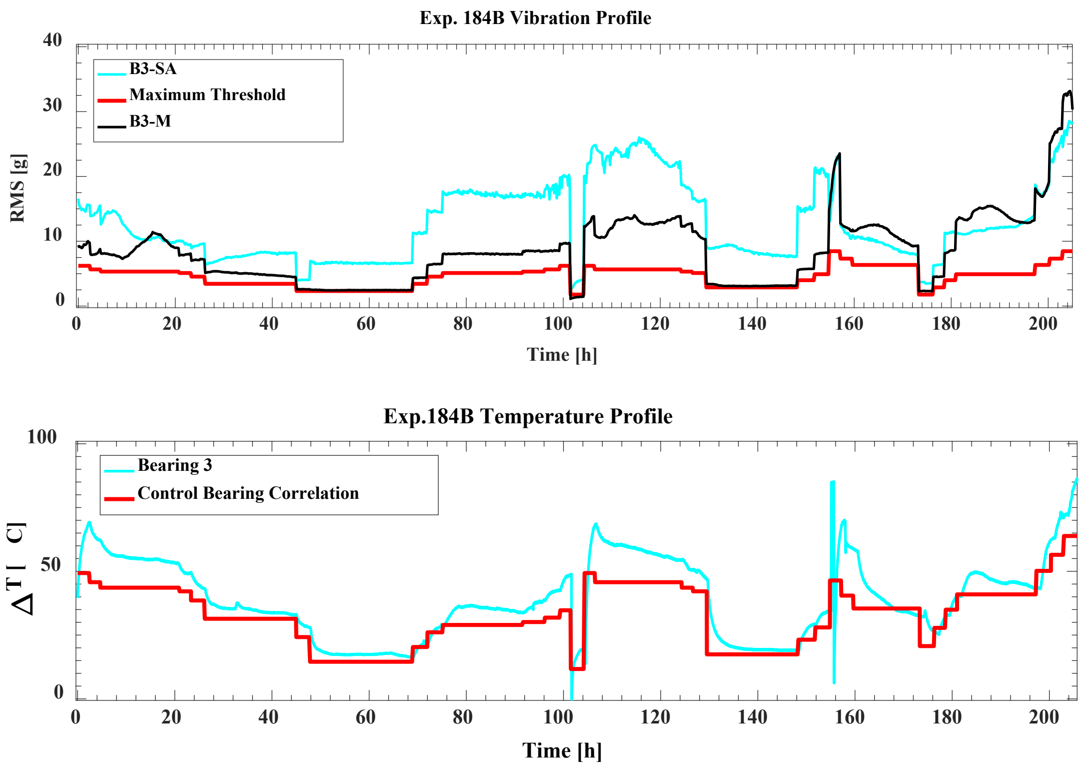

Figure 34. Vibration and temperature profiles for Experiment 184B

Using the RMS of 27 g, a defect area of 57 cm^2 was calculated. The theoretical defect size had a 92% accuracy to the actual. The upper and lower growth rate bounds calculated through the RMS yielded values of 10.9E-04 cm^2/km and 0.3E-04 cm^2/km, respectively. The actual growth rate of 6.1E-04 cm^2/km falls well within the margin formed by these two boundaries, as can be seen in Figure 35.

Table 7. Average values for the final two hours of Experiment 184B

Experiment 184B (Bearing 2 Cup Spall)			
Track Speed [km/h]/[mph]	Load [%]	ΔT [°C / °F]	RMS [g]
137 / 85	100	86 / 187	27

Table 8. Spall size and spall growth rate values for Experiment 184B

RMS	Defect Size [cm^2]	Calculated Defect Size [cm^2]	Accuracy [%]
27	53	57	92
	Lower Bound Growth Rate [cm^2 / km] * 10^{-4}	**Actual Growth Rate [cm^2 / km] * 10^{-4}**	**Upper Bound Growth Rate [cm^2 / km] * 10^{-4}**
	0.3	6.1	10.9

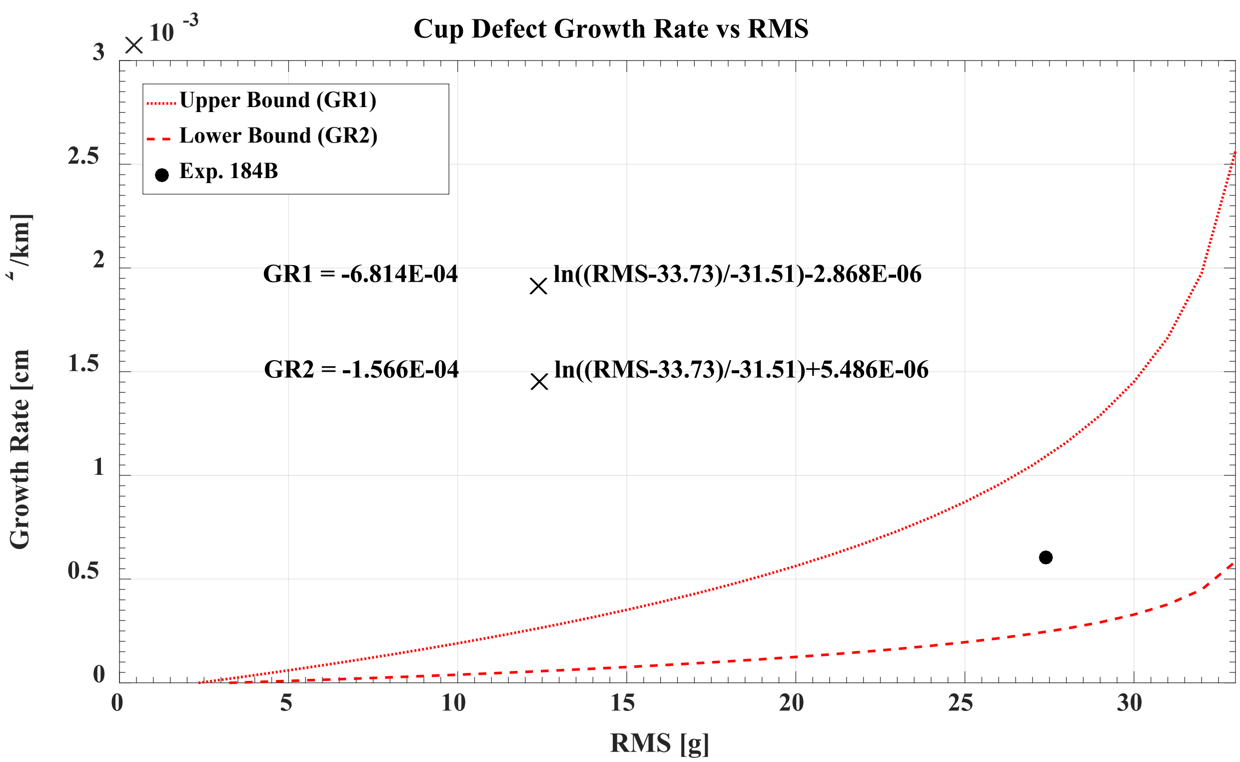

Figure 35. Experiment 184B settled in cup spall growth rate regression model

Since the initial cone defect yielded an RMS value of 16 g in Experiment 184A, it was categorized as a yellow indication (monitor condition). Looking back at Table 4, the residual life of a spall categorized within an 8 - 17 g RMS value has a range of 40,000 - 80,000 km (25,000 -

50,000 miles). Experiment 184B lies within this residual life estimate, taking a total of 47,000 km (29,000 mi) for a yellow indication to reach its service life (red indication)

4.3.3 Laboratory Experiment 202A: Cone Defect

In Experiment 202A, a defective cone with a spall area of 9 cm^2 (1.4 in^2) was placed in the single-bearing tester (SBT) for further defect propagation. The experiment ran under full-speed and full-load conditions for a total of 33,000 km (20,500 mi) in which the spall size grew to 10.5 cm^2 (1.6 in^2). Figure 37 shows the vibration (top) and temperature (bottom) profiles for the duration of the experiment.

Figure 36. Experiment 202A: Initial cone raceway (left) and final cone raceway (right)

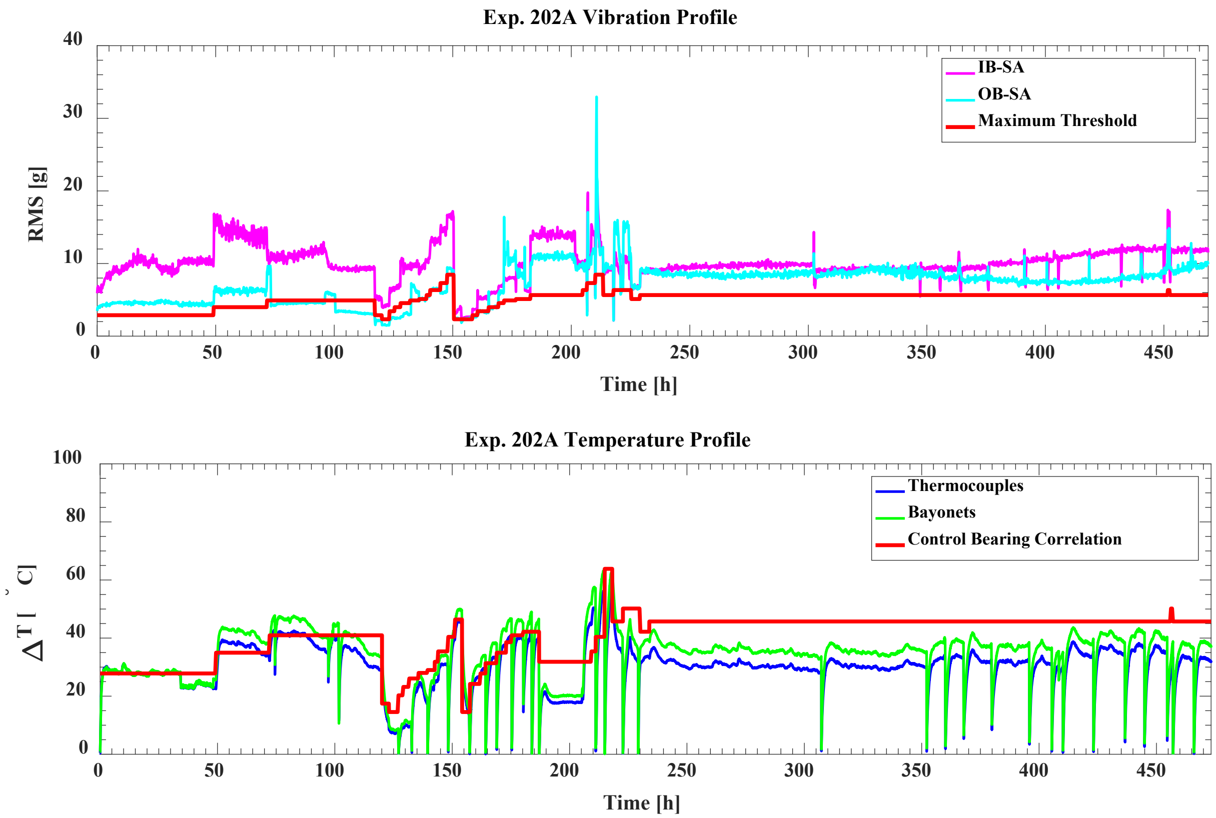

Figure 37. Vibration and temperature profiles for Experiment 202A

An RMS of 11 g was obtained after taking the average of the last two experiment hours for both the inboard (IB) and outboard (OB) SmartAdapter^{TM} (SA) locations. This RMS was used to calculate a 13 cm^2 defect area, which had a 76% accuracy to the true spall size. The shortage of data containing inner ring spall areas above 6.5 cm^2 (1 in^2) can account for the lower confidence in the calculated cone defect size when compared to the outer ring examples provided by Experiment 200 and Experiment 184B. However, when calculating the upper bound and lower bound growth rates, values of 2.3E-04 cm^2/km and 0.3E-04 cm^2/km were obtained, respectively. Therefore, while the confidence level of the theoretical defect area decreased, the RMS versus defect area growth rate regression analysis still proves functional. Figure 38 displays the defect growth rate for Experiment 202A within the margin dictated by the growth rate boundaries formed through the regression analysis.

Table 9. Average values for the final two hours of Experiment 202A

Experiment 202A (Bearing Cone Spall)			
Track Speed [km/h]/[mph]	Load [%]	ΔT [°C / °F]	RMS [g]
137 / 85	100	28 / 83	11

Table 10. Spall size and spall growth rate values for Experiment 202A

RMS	**Defect Size [cm^2]**	**Calculated Defect Size [cm^2]**	**Percent Accuracy [%]**
11	10.5	13	76
	Lower Bound Growth Rate [cm^2 / km] *10^{-4}	**Actual Growth Rate [cm^2 / km] *10^{-4}**	**Upper Bound Growth Rate [cm^2 / km] *10^{-4}**
	0.3	0.5	2.3

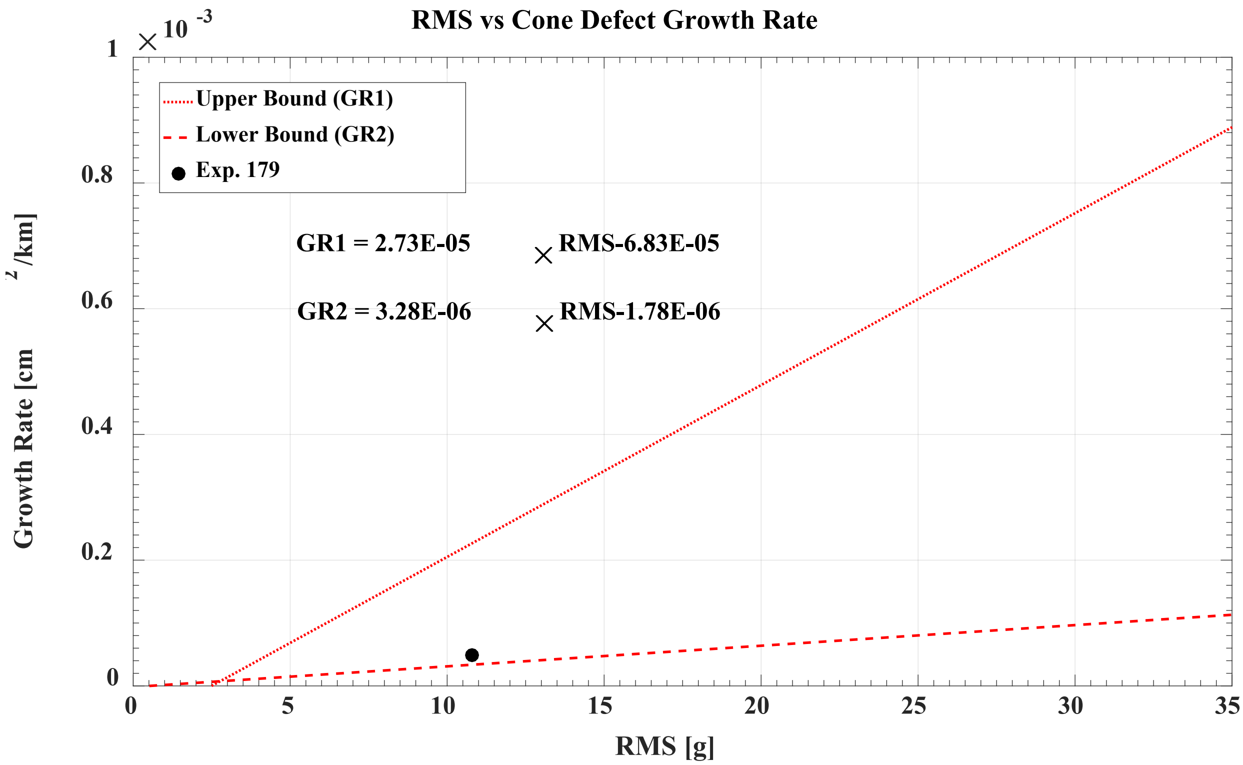

Figure 38. Experiment 202A settled in cone spall growth rate regression model

Although the defect growth rate for Experiment 202A falls closer to the lower bound trendline, the upper bound defect growth rate was still used to resemble a worst-case scenario. Using the upper bound growth rate of 2.3E-04 cm^2/km, it would take approximately 119,000 km (74,000 mi) for the defect to reach 13% of the total inner ring surface area (279 cm^2) and signal a red indication.

4.3.4 Laboratory Experiment 206: Cone Defect

Previously, it was mentioned that cone defects with areas larger than 6.5 cm^2 (1 in^2) were scarce due to the cyclic motion of the component. Therefore, in order to facilitate and ensure thorough defect progression tracking, components with large defect areas are ran in the single-bearing tester (SBT). Experiment 206 consisted of an inner ring with multiple defects containing a total spall area of 36 cm^2 (5.6 in^2), shown in Figure 39. The experiment performed on this component prior to Experiment 206 gave a vibration signature (RMS) of 26 g, categorizing the inner ring as an act condition component (red indication).

Experiment 206 ran full speed and full load conditions on the SBT for a total of 14,000 km (9,000 mi) in which the spall area increased to 39 cm^2 (6 in^2) shown in Figure 40. The experiment was stopped and the bearing was disassembled and inspected once the vibration signatures showed further propagation had occurred. Propagation patterns can be observed in Figure 41 (top) starting from hour 100.

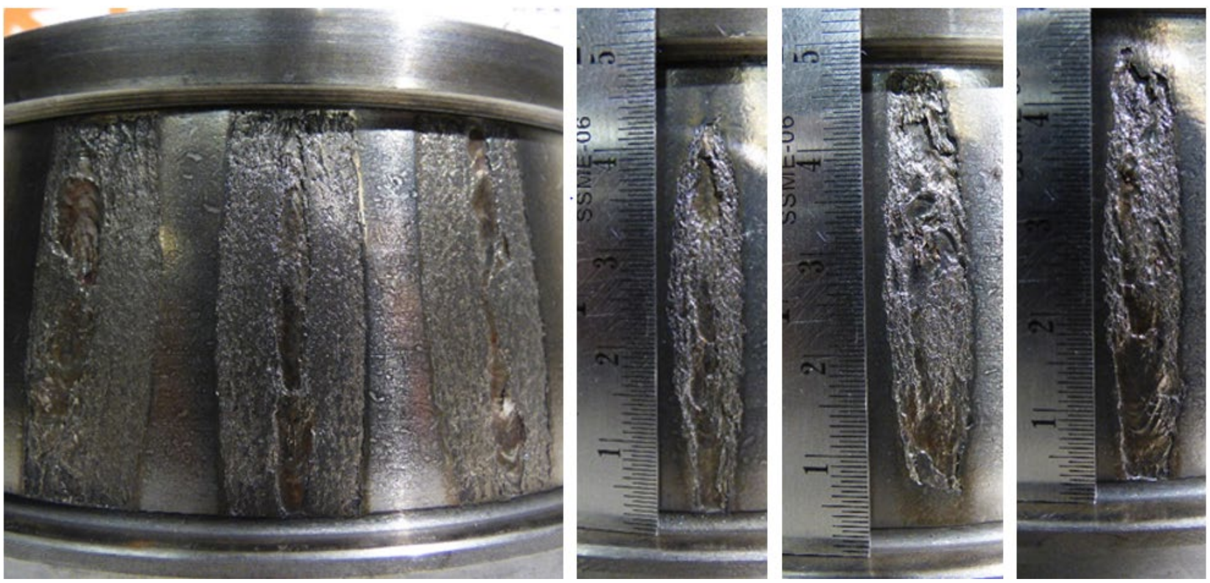

Figure 39. Experiment 206 initial cone raceway (multiple spalls)

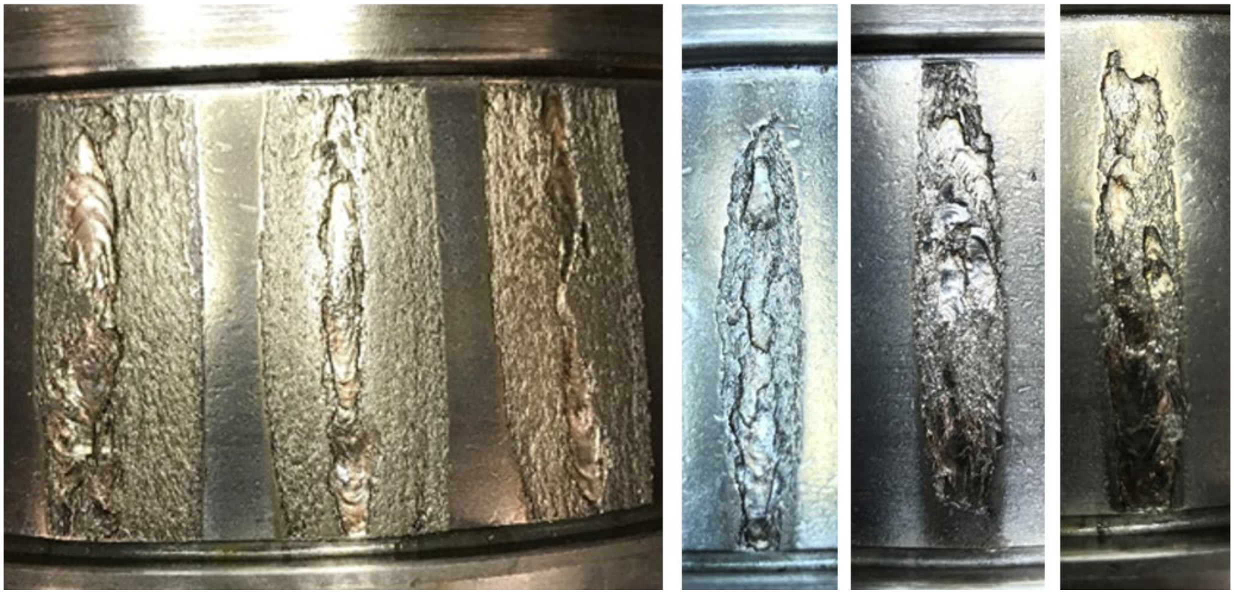

Figure 40. Experiment 206 final cone raceway

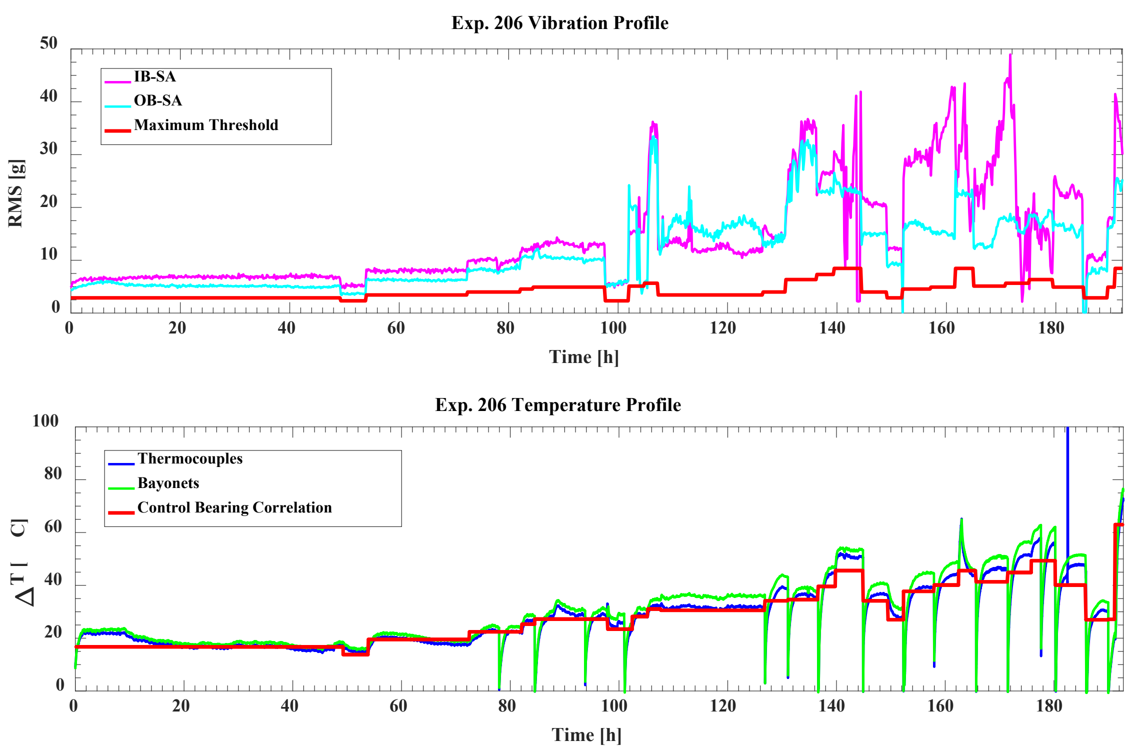

Figure 41. Vibration and temperature profiles for Experiment 206

The inboard (IB) and outboard (OB) SmartAdapter™ vibration signatures were averaged for the last two hours of the experiment, giving an RMS value of 26 g. The RMS obtained was used to calculate the theoretical defect area as well as the upper and lower bound growth rates which can be seen in Table 11 and Table 12, respectively. The calculated defect size, 37 cm^2, had a 95% accuracy to the actual spall area. The higher accuracy in Experiment 206 compared to the inner ring in Experiment 202A can be attributed to the previous explanation given for the larger divergence in the cone regression analysis for spall areas below 6.5 cm^2 (1 in^2), shown as y2 in Figure 19. Spall areas below the 6.5 cm^2 threshold have two possible planes in which to expand. While defects will primarily propagate along the width of the raceway due to rolling contact fatigue (RCF), lateral expansion can still occur, causing a dispersed growth.

The actual growth rate was calculated using the total mileage of the experiment, yielding a value of 1.8E-04 cm^2/km. The upper and lower growth rate bounds were calculated with the RMS of 26 g and resulted in 6.5E-04 cm^2/km and 0.9E-04 cm^2/km, respectively. Figure 42 shows the actual growth rate of Experiment 206 in the growth rate versus RMS regression model. It can be observed that the data falls within the growth rate margins projected.

Table 11. Average values for the final two hours of Experiment 206

Experiment 206 (Bearing Cone Spall)			
Track Speed [km/h]/[mph]	Load [%]	ΔT [°C / °F]	RMS [g]
137 / 85	100	68 / 155	26

Table 12. Spall size and spall growth rate values for Experiment 206

RMS	**Defect Size [cm^2]**	**Calculated Defect Size [cm^2]**	**Percent Accuracy [%]**

26	39	37	95
	Lower Bound Growth Rate [cm² / km] *10⁻⁴	**Actual Growth Rate [cm² / km] *10⁻⁴**	**Upper Bound Growth Rate [cm² / km] *10⁻⁴**
	0.9	1.8	6.5

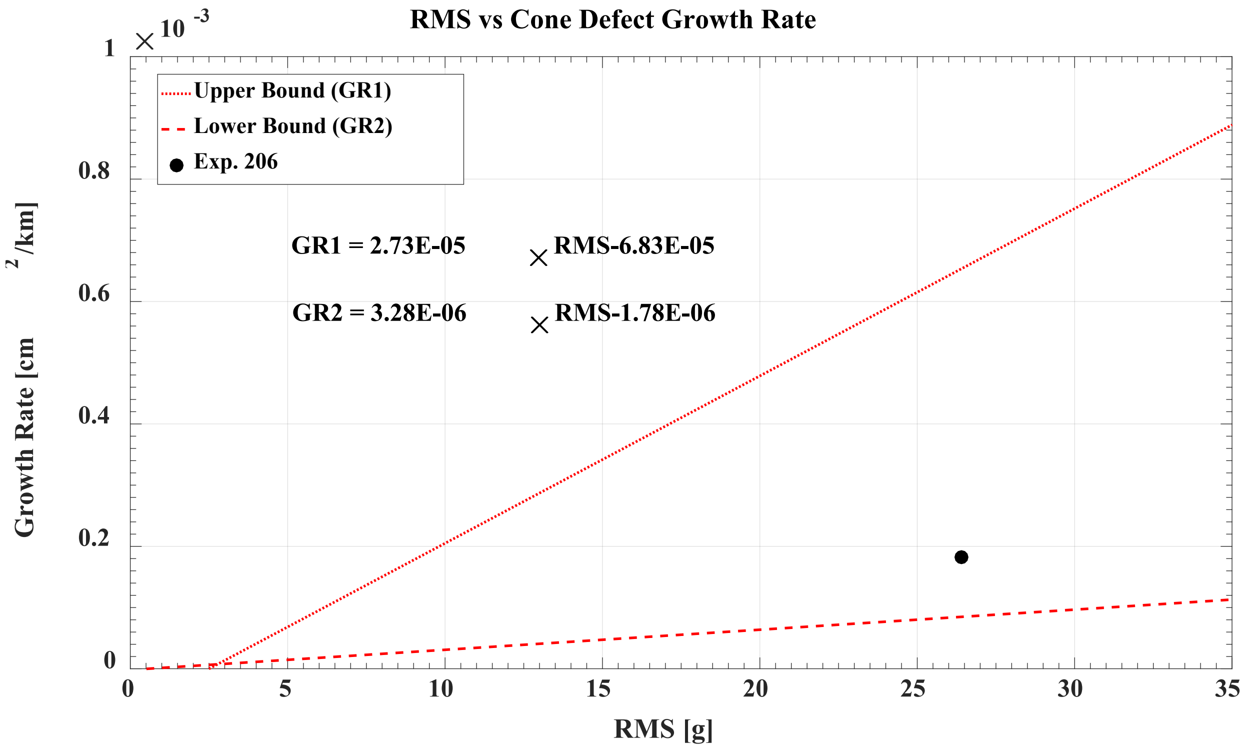

Figure 42. Experiment 206 settled in cone spall growth rate regression model

As previously mentioned, the component used for Experiment 206 had a pre-test RMS value of 26 g causing it to be in an act condition (red indication) with a predicted residual service life of less than 16,000 km (10,000 miles). Experiment 206 was only able to run 14,000 km (9,000 mi) before it was required to be stopped due to propagation. The results from Experiment 206 can further attest for the accuracy of the residual life prognostic models developed.

Comparing the cup and cone laboratory experiment examples it can be noted that the cone defect growth rates fall closer to the lower bound growth rate trend (GR2) while the outer ring (cup) defect growth rates rest along the center of the marked boundary. This pattern can again be attributed to the loading conditions of the tapered roller bearing components. The outer ring (cup) is a static component which keeps a standard load applied while the cone experiences cyclic loading as it rotates with the axle. The cyclic loading in the cone causes slower defect propagation as it doesn’t experience the same constant stresses as the outer ring (cup).

CHAPTER V

CONCLUSION

Train derailments are a significant and widely recognized problem for both environmental and monetary resources in the railroad industry. However, unnecessary stoppages and in-service failures (ISFs) can account for a large portion of the financial waste by creating delays and needless premature maintenance expenditures. These problems are primarily rooted in the bearing health condition monitoring systems currently used in the field. The TADS™ and HBDs wayside condition monitoring systems which, while scarcely found in the field, are the most commonly used in the railroad industry. These detectors are specialized in finding end-of-life bearings prone to causing train derailments but remain ineffective at minimizing ISFs.

The University Transportation Center for Railway Safety (UTCRS) developed SmartAdapter™ in order to provide an effective onboard system for the continuous monitoring of the bearing temperature and vibration profiles. This onboard data acquisition tool works in conjunction with a defect detection algorithm which provides real-time information on defect existence, component location, and approximate size. Defect detection is accomplished through the vibration profile provided by this onboard bearing health monitoring system and has been crucial in developing the residual life prognostic models presented in this thesis.

After further population of the RMS versus defect area models previously developed, the regression analysis was used together with the components growth rate patterns to form relative growth rate boundaries. The growth rate range for a component can be found through the vibration signature of the bearing. Once the RMS values are provided by the onboard condition monitoring system, the prognostic models will calculate worst-case and best-case scenario growth rates for the component in question.

The laboratory experiments provided as examples in Chapter 4 can attest for the accuracy of the residual life prognostic models developed. The enhanced RMS versus defect area regression analysis can calculate the component defect area with significant precision. The same RMS used to obtain a defect size estimate can then be utilized to form a growth rate boundary for the spalled component. The RMS versus defect growth rate models display an initially narrow growth rate boundary which allows for stringent growth rate estimates in spalls with smaller defect areas. However, as seen on example experiments 184B and 206, larger spall areas conform well within the residual life condition parameters displayed in Table 4. Therefore, while the boundaries in the RMS versus defect growth rate regression analysis might allow for a greater variance when estimating larger defect size's growth rate patterns, it was proved that the catalogued condition parameters provide accurate residual life assessments.

Further data acquisition will be useful to continue to populate the regression analysis models used, thus increasing the accuracy of the residual life estimates. Data points for larger defect sizes, particularly for inner ring (cone) components, will help increase the precision in calculating defect size estimates and minimize the divergence between the upper bound and lower bound growth rate curves seen in the RMS versus defect growth rate models.

A proper maintenance schedule for railcar bearings will decrease not only derailments, but also in-service failures (ISFs) and premature maintenance costs. Current bearing health monitoring technology such as TADS™ only detect end-of-life bearings (with defect areas over 90% of the component raceway) which call for immediate action often creating ISFs. The vibration parameters developed for bearing residual life will enable an act condition (red indication) in bearing defects covering 15% of the component raceway and allow up to 16,000 km (10,000 mi) for appropriate maintenance conditions to be prepared, thus preventing ISFs.

With the regression analysis presented for the inner ring (cone) and outer ring (cup) components, a proactive maintenance schedule can be developed, consequently minimizing the occurrence of derailments as well as ISFs and premature maintenance. These residual life models work in conjunction with the Smart Adapter technology developed by the UTCRS research team. Constant monitoring of the bearing's vibration profiles will allow for the detection of onset defect development and proper residual life estimates can be provided through the regression analysis models presented in this thesis. The catalogued condition parameters presented in Table 4 also serve as an overview of the residual life of a component.

REFERENCES

[1] Liu, Xiang, M. RapikSaat, and Christopher PL Barkan. "Analysis of causes of major train derailment and their effect on accident rates." Transportation Research Record 2289.1 (2012): 154-163.

[2] https://www.schaeffler.my/remotemedien/media/_shared_media/08_media_library/01_publications/schaeffler_2/brochure/downloads_1/pbs_de_en.pdf

[3] Office of Safety Analysis, FRA, U.S. Department of Transportation. Sec. 3.01–3.04, 9.01, and 9.05. http://safetydata.fra.dot.gov/officeofsafety/. Accessed Jan. 30, 2020.

[4] Schlake, Bryan W., Christopher PL Barkan, and J. Riley Edwards. "Train delay and economic impact of in-service failures of railroad rolling stock." Transportation research record 2261.1 (2011): 124-133.

[5] Anderson, Gerald B. "Acoustic detection of distressed freight car roller bearings." ASME/IEEE 2007 Joint Rail Conference and Internal Combustion Engine Division Spring Technical Conference. American Society of Mechanical Engineers Digital Collection, 2007.

[6] An Implementation Guide for Wayside Detector Systems. (n.d.). Retrieved January 30, 2020, from http://www.trb.org/Main/Blurbs/179225.aspx

[7] Southern, Carolyne, David Rennison, and Uwe Kopke. "RailBAM-An advanced bearing acoustic monitor: initial operational performance results." CORE 2004: New Horizons for Rail (2004): 23.

[8] Ose, Mixanikos. "Heat Detectors-box and Brake Disc (Hot Box & Hot Wheel Detection System)." *Heat Detectors-box and Brake Disc (Hot Box & Hot Wheel Detection System)*. N.p., 16 July 2015. Web.

[9] A. Mealer, C. Tarawneh, S. Crown, Radiative Heat Transfer Analysis of Railroad Bearings for Wayside Hot-box Detector Optimization. *Proceedings of the 2017 Joint Rail Conference,* Philadelphia, PA, April 4-7, 2017.

[10] J. Aranda, "Radiative Heat Transfer Analysis of Railroad Bearings for Wayside Thermal Detector Optimization," Master's Thesis, Department of Mechanical Engineering, The University of Texas Rio Grande Valley, December 2018.

[11] C. Tarawneh, J. Aranda, V. Hernandez, S. Crown and J. Montalvo. "An investigation into wayside hot-box detector efficacy and Optimization," *International Journal of Rail*

Transportation, under review, submitted March 2019.

[12] J. G. Tabbachi, R. R. Newman, R. C. Leedham, D. A. Purta, G. G. Madered and R. Galli, "Hot Bearing Detection with the SMART-BOLT," Proceedings of the 1990 ASME/IEEE Joint Railroad Conference, p. 105-10, 1990.

[13] Tarawneh, Constantine M., et al. "A Vibration Energy Approach Used to Identify Temperature Trending in Railroad Tapered-Roller Bearings." International Journal of Acoustics & Vibration 20.2 (2015).

[14] Wilson, Brent M., and Martin, Andrew. "Bearing Condition Monitoring Using Wireless Technology to Reduce the Risk of Bearing Failure." Proceedings of the ASME 2012 Rail Transportation Division Fall Technical Conference. ASME 2012 Rail Transportation Division Fall Technical Conference. Omaha, Nebraska, USA. October 16–18, 2012. pp. 213-222. ASME.`

[15] J. A. Turner, B. M. Wilson, and L. Koester*. Service life testing of railroad bearings with known subsurface inclusions detected with advanced ultrasonic technology. Int. J. of Railway Technology, Vol. 2, No. 3, pp. 55-78, 2013.

[16] A. Gonzalez, "Development, Optimization, and Implementation of a Vibration Based Defect Detection Algorithm for Railroad Bearings," Master's Thesis, The University of Texas Rio Grande Valley, August 2015.

[17] Montalvo, J., "Defect Detection Algorithm Optimization for Use in Freight Railcar Service," Master's Thesis, The University of Texas Rio Grande Valley, August 2019.

[18] De Los Santos, N., Tarawneh, C., Jones, R., and Fuentes, A., "Defect Prognostic Models for Spall Growth in Railroad Bearing Rolling Elements," Proceedings of the 2018 ASME Joint Rail Conference, Pittsburgh, PA, April 18-20, 2018.

[19] Jamison, W. E., J. J. Kauzlarich, and E. V. Mochel. "Geometric effects on the rib-roller contact in tapered roller bearings." AsLE Transactions 20.1 (1977): 79-88.

[20] C. Tarawneh, J. Lima, N. De Los Santos, and R. Jones. "Prognostics models for railroad tapered-roller bearings with spall defects on inner or outer rings," Tribology Transactions, accepted for publication, submitted February 2019.

[21] "HERTZIAN CONTACT STRESS CALCULATOR." Hertzian Contact Stress Calculator, amesweb.info/HertzianContact/HertzianContact.aspx.

[22] J. Montalvo, C. Tarawneh, J. Lima, J. Cuanang, and N. De Los Santos, "Estimating the outer ring defect size and remaining service life of freight railcar bearings using vibration signatures," Proceedings of the 2019 ASME Joint Rail Conference, Snowbird, UT, April 9-12, 2019.

BIOGRAPHICAL SKETCH

Jennifer Danni Lima was born in San Juan, Texas. She is the youngest of three siblings. She went to Thomas Jefferson Early College Highschool. Later, she attended the University of Texas Pan American which became the University of Texas Rio Grande Valley, where she graduated Cum Laude with a Civil Engineering Degree. She earned her Master's in Mechanical Engineering in May 2020. Jennifer has accepted a job offer at Raytheon in McKinney, Texas. Jennifer can be contacted through her personal email jenniferdanni@live.com.